Available online at www.sciencedirect.com
SCIENCE DIRECT®
Comput. Methods Appl. Mech. Engrg. 192 (2003) 1227–1258
Computer methods in applied mechanics and engineering
www.elsevier.com/locate/cma

# On the numerical integration of three-invariant elastoplastic constitutive models

Ronaldo I. Borja *, Kossi M. Sama, Pablo F. Sanz

*Department of Civil and Environmental Engineering, Stanford University, Stanford, CA 94305, USA*

Received 15 May 2002; received in revised form 23 September 2002

**Abstract**

We investigate the performance of a numerical algorithm for the integration of isotropically hardening three-invariant elastoplastic constitutive models with convex yield surfaces. The algorithm is based on a spectral representation of stresses and strains for infinitesimal and finite deformation plasticity, and a return mapping in principal stress directions. Smooth three-invariant representations of the Mohr–Coulomb model, such as the Lade–Duncan and Matsuoka–Nakai models, are implemented within the framework of the proposed algorithm. Among the specific features incorporated into the formulation are the hardening/softening responses and the tapering of the yield surfaces toward the hydrostatic axis with increasing confining pressure. Isoerror maps are generated to study the local accuracy of the numerical integration algorithm. Finally, a boundary-value problem involving loading of a strip foundation on a soil is analyzed with and without finite deformation effects to investigate the performance of the integration algorithm in a full-scale non-linear finite element simulation.


## 1. Introduction

Plasticity models for frictional materials such as concrete, soil and rock are most conveniently represented in principal stress space. The general characteristics of the yield surface are described by its cross-sectional shape on the deviatoric plane and its trace on meridian planes. In frictional materials the form of the failure envelope is significantly affected by the value of the confining pressure. On a meridian plane the shape of the failure surface can curve like a parabola, while on the deviatoric plane the shape can vary from a curvilinear triangle at low confining pressures to nearly circular at high confining pressures [1].

A classical plasticity model that takes into account the shape of the failure surface on the deviatoric plane is the Mohr–Coulomb (MC) model. Widely used for representing the yield and failure behavior of cohesive-frictional materials, this model has the shape of an irregular hexagon on the deviatoric plane and predicts a higher yield/failure strength in compression than in tension. Whereas this model is relatively easy to

* Corresponding author. Fax: +1-650-723-7514.
*E-mail address:* borja@stanford.edu (R.I. Borja).

0045-7825/03/$ - see front matter 
doi:10.1016/S0045-7825(02)00620-5

implement in a two-dimensional loading condition, the presence of corners makes the MC model less straightforward to implement in a general three-dimensional framework. Moreover, on a meridian plane the shape of the failure/yield surface is a straight line for a constant value of the friction angle, which may not be realistic for some frictional materials like concrete.

Smooth yield surfaces that very much resemble the shape of the MC surface on the deviatoric plane have been proposed in the literature to avoid the difficult problem of yielding at a corner. Clearly, these models must be functions of all three stress invariants to capture the pressure-dependency and the irregular cross-sectional shape of the surface on the deviatoric plane. Smooth three-invariant models for frictional materials include the Lade–Duncan (LD) [2] and Matsuoka–Nakai (MN) [3] models, among others (see also [4–6]). Additional enhancements may be introduced in these plasticity models to capture the curved shape of the yield/failure surface on the meridian plane [7].

Apart from the complexities of the yield and plastic potential surfaces in principal stress axes, one has to deal with an obvious problem that the principal stress axes themselves may rotate. In describing the evolution of the plastic responses, the rotation of the principal stress axes must be considered explicitly in the formulation of tensorial models of plasticity. When implemented in a large-scale finite element analysis this creates an enormous difficulty not encountered with simpler plasticity models such as the von Mises $J_2$ and the two-invariant Drucker–Prager plasticity models.

The objective of this paper is to implement a class of stress-point integration algorithms appropriate for three-invariant isotropically hardening plasticity models that explicitly accounts for the rotation of principal stress axes. The formulation is based on a spectral representation of stresses and strains and a return mapping in the principal stress (or strain) axes. The notion of return mapping in principal stress directions is not new – Simo [8,9] utilized this approach to implement a product formula algorithm for finite deformation multiplicative plasticity. His choice of this approach, however, was motivated primarily by the problem of geometric non-linearity and not by the complexity of the constitutive model. In the present paper, we propose to use the same return mapping in principal stress axes to handle the presence of all three stress invariants in the plasticity theory. Many three-invariant plasticity models are conveniently expressed in terms of the principal stresses themselves, so a return mapping in principal axes is a natural way of numerically integrating the elastoplastic rate-constitutive relations in the presence of all three stress invariants.

Among the three-invariant plasticity models investigated in this paper are the MC, LD, and MN plasticity models, widely used for representing the behavior of cohesive-frictional materials such as concrete, soil and rock. The numerical integration of the MC plasticity model is not trivial due to the presence of corner or vertex effects. In this paper we accommodate corner effects using a multisurface plasticity formulation of Koiter [10]. The LD and MN models are two 'smooth' versions of the MC model. There is enough evidence suggesting that these smooth versions in fact capture the mechanical responses of granular materials more accurately than even the MC model itself, thus further motivating their consideration. Here, we combine these two models into a more general representation of a class of smooth three-invariant plasticity models which is numerically integrated using the proposed return mapping algorithm.

A key component of the algorithm is the linearization of the discrete evolution of stresses necessitating an algorithmic tangent operator for use in Newton iteration. Whereas the linearization of stresses for the case of non-rotating principal stress axes results in a unique form for the material component of the tangent operator, at least two forms are possible for the linearization of the 'spin part' characterizing the instantaneous rotation of the principal axes. The first possible linearization of the spin part utilizes the approach proposed by Ogden [11] which requires an explicit evaluation of the eigenvectors $\boldsymbol{n}^{(A)}$, $A = 1, 2, 3$, of the principal stresses. In this paper we shall call this technique the eigenvector linearization approach. A second possible expression for the explicit linearization of the spin part uses a closed-form expression for the eigenbases $\boldsymbol{m}^{(A)} = \boldsymbol{n}^{(A)} \otimes \boldsymbol{n}^{(A)}$ together with the use of some important properties of isotropic fourth-order

tensors [8,9,12–15]. In this paper we shall call this technique the eigenbasis linearization approach. The numerical performances of both the eigenvector and eigenbasis approaches are assessed in this paper.

As for notations and symbols, bold-face letters denote matrices and vectors; the symbol '$\cdot$' denotes an inner product of two vectors (e.g. $\boldsymbol{a}\cdot\boldsymbol{b}=a_ib_i$), or a single contraction of adjacent indices of two tensors (e.g. $\boldsymbol{c}\cdot\boldsymbol{d}=c_{ij}d_{jk}$); the symbol ':' denotes an inner product of two second-order tensors (e.g. $\boldsymbol{c}:\boldsymbol{d}=c_{ij}d_{ij}$), or a double contraction of adjacent indices of tensors of rank two and higher (e.g. $\boldsymbol{C}:\boldsymbol{\epsilon}^{\mathrm{e}}=C_{ijkl}\epsilon^{\mathrm{e}}_{kl}$); the symbol '$\otimes$' denotes a juxtaposition, e.g., $(\boldsymbol{a}\otimes\boldsymbol{b})_{ij}=a_ib_j$. For any symmetric second order tensors $\boldsymbol{\alpha}$ and $\boldsymbol{\beta}$, we have $(\boldsymbol{\alpha}\otimes\boldsymbol{\beta})_{ijkl}=\alpha_{ij}\beta_{kl}$; $(\boldsymbol{\alpha}\oplus\boldsymbol{\beta})_{ijkl}=\alpha_{jl}\beta_{ik}$; and $(\boldsymbol{\alpha}\ominus\boldsymbol{\beta})_{ijkl}=\alpha_{il}\beta_{jk}$.

## 2. Return mapping algorithm for infinitesimal plasticity

In this section we review the return-mapping algorithm in principal directions for small deformation elastoplasticity. In the next section, we focus on the numerical implementation of a number of specific three-invariant plasticity models.

### 2.1. General formulation

Our point of departure is the variational form of the linear momentum balance equation, which, for quasistatic loading, reads

$$\mathscr{W}=\int_\Omega(\operatorname{grad}\boldsymbol{\eta}:\boldsymbol{\sigma}-\rho\boldsymbol{\eta}\cdot\mathbf{g})\,\mathrm{d}V-\int_{\partial\Omega}\boldsymbol{\eta}\cdot\boldsymbol{t}\,\mathrm{d}A=0, \tag{2.1}$$

where $\boldsymbol{\sigma}$ is the Cauchy stress tensor, $\rho$ is the mass density, $\mathbf{g}$ is the vector of gravity accelerations, $\boldsymbol{t}$ is the traction vector, $\boldsymbol{\eta}$ is the weighting function, $\Omega$ is the domain of integration, and $\partial\Omega$ is the domain boundary. For dead loading the linearization of this function with respect to the state $\mathscr{W}^0$ reads

$$L\mathscr{W}=\mathscr{W}^0+\int_\Omega\operatorname{grad}\boldsymbol{\eta}:\mathbf{c}:\operatorname{grad}\delta\boldsymbol{u}\,\mathrm{d}V-\int_{\partial\Omega}\boldsymbol{\eta}\cdot\delta\boldsymbol{t}\,\mathrm{d}A, \tag{2.2}$$

where $\boldsymbol{u}$ is the displacement field. Here, $\mathbf{c}$ is a tangent operator consistent with the linearization of $\boldsymbol{\sigma}$.

We assume a stress evolution $\boldsymbol{\sigma}_t$ emanating from a standard strain-driven problem. The displacement and strain fields driving the problem are given, respectively, by

$$\boldsymbol{u}_t:\boldsymbol{\varphi}_n(\Omega)\times[t_n,t_{n+1}]\to R^3,\qquad\boldsymbol{\epsilon}_t=\operatorname{sym}(\nabla\boldsymbol{u}_t)\in S, \tag{2.3}$$

where $\boldsymbol{\varphi}_n$ is the configuration at time $t_n$ and $S$ is the space of symmetric second-order tensors. A specific form for $\boldsymbol{\sigma}_t$ in the context of elastoplasticity is given by the return mapping equation

$$\boldsymbol{\sigma}_t=\boldsymbol{\sigma}_t^{\mathrm{tr}}-\Delta\lambda_t\boldsymbol{c}^{\mathrm{e}}:\boldsymbol{g}_t, \tag{2.4}$$

where $\boldsymbol{\sigma}_t^{\mathrm{tr}}$ is the trial elastic stress predictor, $\Delta\lambda_t$ is the discrete plastic multiplier, and

$$\boldsymbol{g}_t=\frac{\partial G}{\partial\boldsymbol{\sigma}_t},\quad G=G(\boldsymbol{\sigma}_t,\boldsymbol{\kappa}_t) \tag{2.5}$$

is the gradient to the plastic potential function $G$, with $\boldsymbol{\kappa}_t$ representing a vector of plastic internal variables. The assumption here is that we are given initial values $\boldsymbol{\sigma}_n$ and $\boldsymbol{\kappa}_n$, and the problem is to find the evolution of these variables over the interval $t\in[t_n,t_{n+1}]$.

We recall the spectral representation

$$\boldsymbol{\sigma}_t = \sum_{A=1}^{3} \sigma_A \boldsymbol{m}^{(A)}, \qquad \boldsymbol{m}^{(A)} = \boldsymbol{n}^{(A)} \otimes \boldsymbol{n}^{(A)}, \tag{2.6}$$

where $\sigma_A$ and $\boldsymbol{n}^{(A)}$ are the principal Cauchy stress and principal direction, respectively. If isotropy in the elastic response is assumed, then we have

$$\boldsymbol{\epsilon}_t^{\mathrm{e}} = \boldsymbol{\epsilon}_n^{\mathrm{e}} + \Delta\boldsymbol{\epsilon}_t^{\mathrm{e}} = \sum_{A=1}^{3} \epsilon_A^{\mathrm{e}} \boldsymbol{m}^{(A)}, \tag{2.7}$$

i.e., the spectral directions of $\boldsymbol{\epsilon}_t^{\mathrm{e}}$ coincide with those of $\boldsymbol{\sigma}_t$. In this case, the gradients of any scalar functions of stress invariants, such as the yield and plastic potential functions $F$ and $G$, may be evaluated as

$$\frac{\partial F}{\partial \boldsymbol{\sigma}} = \sum_{A=1}^{3} \frac{\partial F}{\partial \sigma_A} \boldsymbol{m}^{(A)}, \qquad \frac{\partial G}{\partial \boldsymbol{\sigma}} = \sum_{A=1}^{3} \frac{\partial G}{\partial \sigma_A} \boldsymbol{m}^{(A)}, \tag{2.8}$$

with $\boldsymbol{m}^{(A)}$ being a spectral direction of $\boldsymbol{\epsilon}_t^{\mathrm{e}}$ as well.

With isotropy the spectral directions of the trial elastic strain tensor $\boldsymbol{\epsilon}_t^{\mathrm{e\,tr}} := \boldsymbol{\epsilon}_n^{\mathrm{e}} + \Delta\boldsymbol{\epsilon}_t$ also coincide with those of $\boldsymbol{\sigma}_t$. This means that the return mapping algorithm may be formulated in principal stress space, a mathematical convenience, and the relevant expression in principal stress space takes the form

$$\sigma_A = \sigma_A^{\mathrm{tr}} - \Delta\lambda_t \sum_{B=1}^{3} a_{AB}^{\mathrm{e}} \frac{\partial G}{\partial \sigma_B}, \quad A = 1, 2, 3, \tag{2.9}$$

where

$$[a_{AB}^{\mathrm{e}}] = \begin{bmatrix} \lambda_{\mathrm{L}} + 2\mu & \lambda_{\mathrm{L}} & \lambda_{\mathrm{L}} \\ \lambda_{\mathrm{L}} & \lambda_{\mathrm{L}} + 2\mu & \lambda_{\mathrm{L}} \\ \lambda_{\mathrm{L}} & \lambda_{\mathrm{L}} & \lambda_{\mathrm{L}} + 2\mu \end{bmatrix}$$

is the matrix of elastic moduli, $\lambda_{\mathrm{L}}$ is the Lamé parameter, and $\mu$ is the elastic shear modulus. In addition, the evolution of the plastic internal variables is given by

$$\boldsymbol{\kappa}_t = \boldsymbol{\kappa}_n + \Delta\boldsymbol{\kappa}_t. \tag{2.10}$$

Finally the discrete consistency condition must be satisfied on yielding,

$$F(\sigma_1, \sigma_2, \sigma_3, \boldsymbol{\kappa}_t) = 0. \tag{2.11}$$

The last three equations may be solved in principle to determine the evolution of the principal stresses $\sigma_A$, the plastic internal variables $\boldsymbol{\kappa}_t$ and the discrete plastic multiplier $\Delta\lambda_t$. The evolution of the complete stress tensor may be obtained from the spectral representation (2.6), where the directions $\boldsymbol{m}^{(A)}$ are determined explicitly from the spectral decomposition of $\boldsymbol{\epsilon}_t^{\mathrm{e\,tr}}$.

A summary of the return mapping algorithm in principal stress axes for an isotropically hardening three-invariant plasticity model is shown in Box 1. Here, $\boldsymbol{c}^{\mathrm{e}}$ is the fourth-order elasticity tensor. For non-linear hardening and non-planar plastic potential function the solution of the discrete consistency condition, Step 4, may require an iterative process and may have to be done simultaneously with Steps 5 and 6. Note that the spectral decomposition of $\boldsymbol{\sigma}_t^{\mathrm{tr}}$ (or $\boldsymbol{\epsilon}_t^{\mathrm{e\,tr}}$) requires the solution of an eigenvalue problem; for three-dimensional problems this entails the solution of a cubic equation in closed-form. The elements of the vector of plastic internal variables $\boldsymbol{\kappa}_t$ are not necessarily all 'stress-like' in nature—for example, a friction hardening law may lead to an element of $\boldsymbol{\kappa}$ in the form of a tangent of the friction angle.

Box 1. Return mapping algorithm in principal stress axes for isotropically hardening three-invariant plasticity model, infinitesimal case

Step 1. Compute $\boldsymbol{\sigma}_t^{\mathrm{tr}} = \boldsymbol{\sigma}_n + \boldsymbol{c}^{\mathrm{e}} : \Delta\boldsymbol{\epsilon}_t$
Step 2. Spectrally decompose $\boldsymbol{\sigma}_t^{\mathrm{tr}} = \sum_{A=1}^{3} \sigma_A^{\mathrm{tr}} \boldsymbol{m}^{\mathrm{tr}(A)}$
Step 3. Check $F(\sigma_1^{\mathrm{tr}}, \sigma_2^{\mathrm{tr}}, \sigma_3^{\mathrm{tr}}, \boldsymbol{\kappa}_n) > 0$? No, set $\boldsymbol{\sigma}_t = \boldsymbol{\sigma}_t^{\mathrm{tr}}$ and exit.
Step 4. Yes, solve $F(\Delta\lambda_t) = 0$ for $\Delta\lambda_t$
Step 5. Compute $\sigma_A = \sigma_A^{\mathrm{tr}} - \Delta\lambda_t \sum_{B=1}^{3} a_{AB}^{\mathrm{e}} \partial G / \partial \sigma_B$
Step 6. Update $\boldsymbol{\sigma}_t = \sum_{A=1}^{3} \sigma_A \boldsymbol{m}^{\mathrm{tr}(A)}$, $\boldsymbol{\kappa}_t = \boldsymbol{\kappa}_n + \Delta\boldsymbol{\kappa}_t$ and exit.

### 2.2. Algorithmic tangent operator and spin of principal axes

Proper construction of the consistent tangent operator is very critical for the algorithm to work in a general boundary-value problem. It is known that only with a consistent tangent operator can the algorithm capture the asymptotic rate of quadratic convergence of Newton iteration. In this section we discuss two possible forms for the consistent tangent operator relevant to the proposed return mapping algorithm. In the absence of round-off errors the two forms theoretically should yield the same optimal results.

#### 2.2.1. Form 1: Tangent operator constructed from eigenbases

The consistent tangent operator $\mathbf{c}$ represents the instantaneous variation of the stress tensor $\boldsymbol{\sigma}_t$ with respect to the strain tensor $\boldsymbol{\epsilon}_t$, i.e.,

$$\mathbf{c} = \frac{\partial \boldsymbol{\sigma}_t}{\partial \boldsymbol{\epsilon}_t} \iff \delta\boldsymbol{\sigma}_t = \mathbf{c} : \delta\boldsymbol{\epsilon}_t. \tag{2.12}$$

Since $\delta\boldsymbol{\epsilon}_t = \delta\boldsymbol{\epsilon}_t^{\mathrm{e\,tr}}$, we can derive a closed-form expression for $\mathbf{c}$ by differentiating (2.6) directly with respect to $\boldsymbol{\epsilon}_t^{\mathrm{e\,tr}}$ to get

$$\mathbf{c} = \sum_{A=1}^{3} \sum_{B=1}^{3} a_{AB} \boldsymbol{m}^{(A)} \otimes \boldsymbol{m}^{(B)} + \sum_{A=1}^{3} \sigma_A \boldsymbol{\omega}^{(A)}, \tag{2.13}$$

where $a_{AB} = \partial\sigma_A / \partial\epsilon_B^{\mathrm{e\,tr}}$ is the tangent operator consistent with the return mapping in principal stress directions, and $\boldsymbol{\omega}^{(A)} = \partial \boldsymbol{m}^{(A)} / \partial \boldsymbol{\epsilon}_t^{\mathrm{e\,tr}}$ is a fourth-order tensor reflecting the changing orientation of the spectral directions. The first term of $\mathbf{c}$ is a function of the constitutive response and the algorithm used to track this response, whereas the second term is a function of the rotation of the principal directions alone and not of the specific plasticity model used.

A closed form expression is available for the spectral direction (or eigenbasis) $\boldsymbol{m}^{(A)}$ of any symmetric real-valued second-order tensor $\boldsymbol{e}$ (in the present case, we can simply take $\boldsymbol{e} \equiv \boldsymbol{\epsilon}_t^{\mathrm{e\,tr}}$). The closed-form expression is given in [12,13] as

$$\boldsymbol{m}^{(A)} = \frac{\boldsymbol{e}^2 - (I_1 - e_A)\boldsymbol{e} + I_3 e_A^{-1} \mathbf{1}}{D_A}, \tag{2.14}$$

where

$$D_A := 2e_A^2 - I_1 e_A + I_3 e_A^{-1} \neq 0, \tag{2.15}$$

$e_A$ is the eigenvalue corresponding to the eigenbasis $\boldsymbol{m}^{(A)}$, and $I_1$ and $I_3$ are the first and third invariants of $\boldsymbol{e}$, respectively. Direct differentiation of $\boldsymbol{m}^{(A)}$ with respect to $\boldsymbol{e}$ gives the tangential spin of the principal axis

$$\begin{aligned}\boldsymbol{\omega}^{(A)} = [&\boldsymbol{I}_e - (I_1 - e_A)\boldsymbol{I} - \boldsymbol{e}\otimes\boldsymbol{1} + \boldsymbol{e}\otimes\boldsymbol{m}^{(A)} + I_3 e_A^{-1}\boldsymbol{1}\otimes\boldsymbol{e}^{-1} - I_3 e_A^{-2}\boldsymbol{1}\otimes\boldsymbol{m}^{(A)} \\ &+ e_A\boldsymbol{m}^{(A)}\otimes\boldsymbol{1} - I_3 e_A^{-1}\boldsymbol{m}^{(A)}\otimes\boldsymbol{e}^{-1} + \psi\boldsymbol{m}^{(A)}\otimes\boldsymbol{m}^{(A)}]/D_A,\end{aligned} \tag{2.16}$$

where

$$\begin{aligned}&\boldsymbol{I}_e = \boldsymbol{e}\oplus\boldsymbol{1} + \boldsymbol{e}\ominus\boldsymbol{1} = \boldsymbol{1}\oplus\boldsymbol{e} + \boldsymbol{1}\ominus\boldsymbol{e}, \\ &\psi = I_1 + I_3 e_A^{-2} - 4e_A,\end{aligned} \tag{2.17}$$

and where the symbols $\oplus$ and $\ominus$ are as defined in Section 1.

In using the above analytical expression for $\boldsymbol{\omega}^{(A)}$ it is assumed that the eigenvalues are all distinct and non-zero, otherwise, for the case of repeated roots some perturbation may be necessary to avoid an indeterminate solution. Note that to derive the tangential spin $\boldsymbol{\omega}^{(A)}$ it is only necessary to determine the eigenvalues $e_A$ and not the eigenvectors $\boldsymbol{n}^{(A)}$, since a closed-form solution is available for the eigenbases $\boldsymbol{m}^{(A)}$ via (2.14). Closed-form expressions are available for the eigenvalues of a symmetric second-order tensor, see, for example, the program PRINC on p. 762 of [16]. Theoretically, in the absence of round-off errors, the expression (2.14) for the eigenbases $\boldsymbol{m}^{(A)}$ should yield the same result as that derived directly from the construction of $\boldsymbol{n}^{(A)}\otimes\boldsymbol{n}^{(A)}$.

*2.2.2. Form 2: Tangent operator constructed from eigenvectors*

Alternately, the tangent operator $\mathbf{c}$ may be represented in terms of both the eigenvalues and eigenvectors, as proposed in [11]. The alternative expression takes the form

$$\mathbf{c} = \sum_{A=1}^{3}\sum_{B=1}^{3} a_{AB}\boldsymbol{m}^{(A)}\otimes\boldsymbol{m}^{(B)} + \frac{1}{2}\sum_{A=1}^{3}\sum_{B\neq A}\left(\frac{\sigma_B - \sigma_A}{\epsilon_B^{\mathrm{e\,tr}} - \epsilon_A^{\mathrm{e\,tr}}}\right)\left(\boldsymbol{m}^{(AB)}\otimes\boldsymbol{m}^{(AB)} + \boldsymbol{m}^{(AB)}\otimes\boldsymbol{m}^{(BA)}\right), \tag{2.18}$$

where

$$\boldsymbol{m}^{(A)} = \boldsymbol{n}^{(A)}\otimes\boldsymbol{n}^{(A)}, \quad \boldsymbol{m}^{(AB)} = \boldsymbol{n}^{(A)}\otimes\boldsymbol{n}^{(B)}, \qquad A\neq B. \tag{2.19}$$

The first term in (2.18) is identical to that in (2.13), but the second term utilizes a formulation based on the spin of the principal axes. When comparing the two expressions for $\mathbf{c}$, note that (2.13) only requires an explicit calculation of the eigenbases $\boldsymbol{m}^{(A)}$, whereas (2.18) requires an evaluation of the eigenvectors $\boldsymbol{n}^{(A)}$. Also note that for the case of repeated roots the spin component of (2.18) becomes indeterminate. In this case, however, we have a choice of either introducing a perturbation similar to that used in conjunction with (2.13), or replacing the indeterminate expression $(\sigma_A - \sigma_B)/(\epsilon_B^{\mathrm{e\,tr}} - \epsilon_A^{\mathrm{e\,tr}})$ by the expression $\partial(\sigma_A - \sigma_B)/\partial\epsilon_B^{\mathrm{e\,tr}}$ for the case of repeated roots, see [11].

Algorithmic iterative solutions may be employed to calculate both the eigenvalues and the associated eigenvectors of a symmetric second-order tensor. For example, the IMSL subroutines EVLSF/DEVLSF in Fortran PowerStation 90 utilize orthogonal similarity transformations to reduce the tensor to an equivalent symmetric tridiagonal matrix, after which an implicit rational QR algorithm is used to compute the eigenvalues of this tridiagonal matrix. The eigenvectors are then evaluated using the eigenvalues as perfect shifts (see pp. 169 and 172 of [17]). The reduction routine employed in the algorithm is based on the EISPACK routine TRED2, see [18] for the EISPACK routines. This algorithm, advocated and used in [19], provides an alternative approach for determining the principal values and principal directions of a symmetric second-order tensor.

## 3. Application to three-invariant plasticity models

This section considers some of the well-known three-invariant isotropic plasticity models with convex yield surfaces. Most of these models are used to capture the yield behavior of geomaterials (concrete, soils, rocks), which are known to exhibit different yield stresses in tension and compression. The simplest is the MC model, although the presence of corners makes it difficult to implement in a general three-dimensional framework. Smooth approximations to the MC model are also described in this section.

### 3.1. Mohr–Coulomb plasticity model

Consider the following yield function

$$F(\boldsymbol{\sigma}, \boldsymbol{\kappa}) = |\sigma_A - \sigma_B| - 2c\cos\phi + (\sigma_A + \sigma_B)\sin\phi \leqslant 0 \tag{3.1}$$

and plastic potential function

$$G(\boldsymbol{\sigma}, \boldsymbol{\kappa}) = |\sigma_A - \sigma_B| - 2c\cos\psi + (\sigma_A + \sigma_B)\sin\psi, \tag{3.2}$$

where $c$ is the cohesion, $\phi$ the friction angle, and $\psi \leqslant \phi$ is the dilation angle (the inequality ensures a non-negative plastic dissipation). Here we define $\boldsymbol{\kappa} = (c, \phi, \psi)$, $B = 1 + \mathrm{mod}(A, 3)$, and $C = 1 + \mathrm{mod}(B, 3)$. The yield function $F$ constitutes six planes in principal stress space, forming six corners and a common vertex on the tension side of the hydrostatic axis, see Fig. 1. In the following developments we assume that $\phi$ and $\psi$ are constant, but $c$ may vary with plastic deformation.

Except at the vertex, at most two of the six planes comprising the yield function may be active at the same time. We consider two cases.

**Case 1.** One active yield surface.

Assume the following yield function is active:

$$F(\boldsymbol{\sigma}, \boldsymbol{\kappa}) = \zeta_{AB}(\sigma_A - \sigma_B) - 2c\cos\phi + (\sigma_A + \sigma_B)\sin\phi = 0, \tag{3.3}$$

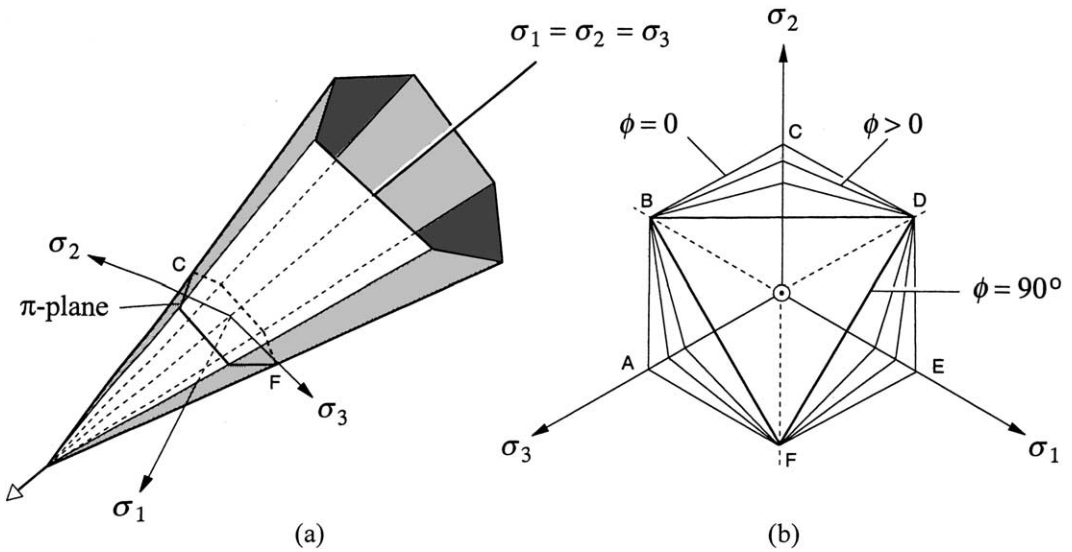


Fig. 1. MC yield functions: (a) principal stress space representation; (b) deviatoric plane representation.

where $\zeta_{AB} = \text{sign}(\sigma_A^{\text{tr}} - \sigma_B^{\text{tr}})$. The corresponding plastic potential function is

$$G(\boldsymbol{\sigma}, \boldsymbol{\kappa}) = \zeta_{AB}(\sigma_A - \sigma_B) - 2c\cos\psi + (\sigma_A + \sigma_B)\sin\psi. \tag{3.4}$$

The gradient of $G$ with respect to a principal stress is

$$\frac{\partial G}{\partial \sigma_I} = \zeta_{AB}(\delta_{AI} - \delta_{BI}) + (\delta_{AI} + \delta_{BI})\sin\psi = \text{constant}, \tag{3.5}$$

where the $\delta$s are the Kronecker delta.

Next, consider the following hardening/softening law

$$\dot{\kappa}_1 = \dot{c} = \frac{H}{2\cos\phi}\dot{\lambda}, \quad \dot{\kappa}_2 = \dot{\phi} = 0, \quad \dot{\kappa}_3 = \dot{\psi} = 0, \tag{3.6}$$

where $H$ is the plastic modulus and $\dot{\lambda} > 0$ is the plastic multiplier. Assuming $H$ is constant, we have the following evolution of the plastic internal variables

$$\boldsymbol{\kappa}_t = \boldsymbol{\kappa}_n + \Delta\boldsymbol{\kappa}_t = \left\{ \begin{array}{c} c_n + H\Delta\lambda_t/(2\cos\phi) \\ \phi \\ \psi \end{array} \right\}. \tag{3.7}$$

Using (2.9) and (3.3), we get

$$\begin{aligned} \Delta\lambda_t &= \frac{1}{\chi}[|\sigma_A^{\text{tr}} - \sigma_B^{\text{tr}}| - 2c_n\cos\phi + (\sigma_A^{\text{tr}} + \sigma_B^{\text{tr}})\sin\phi], \\ \chi &= 4\mu + 4\lambda_{\text{L}}\sin\phi\sin\psi + 4\mu\sin\phi\sin\psi + H. \end{aligned} \tag{3.8}$$

Finally, substituting (3.8) into (2.9) and simplifying, the tangent operator $a_{AB}$ appearing in (2.13) is obtained as

$$a_{AB} = a_{AB}^{\text{e}} - \frac{1}{\chi}\sum_{I=1}^{3}\sum_{J=1}^{3} a_{AI}^{\text{e}}\frac{\partial G}{\partial \sigma_I}\frac{\partial F}{\partial \sigma_J}a_{JB}^{\text{e}}. \tag{3.9}$$

Note that the tangent operator $a_{AB}$ coincides with the elastoplastic constitutive operator suggesting that the algorithm described above is *exact*.

**Case 2.** Two active yield surfaces.

Assume the following yield surfaces are active:

$$\begin{aligned} F_1(\boldsymbol{\sigma}, \boldsymbol{\kappa}) &= \zeta_{AB}(\sigma_A - \sigma_B) - 2c\cos\phi + (\sigma_A + \sigma_B)\sin\phi = 0, \\ F_2(\boldsymbol{\sigma}, \boldsymbol{\kappa}) &= \zeta_{AC}(\sigma_A - \sigma_C) - 2c\cos\phi + (\sigma_A + \sigma_C)\sin\phi = 0, \end{aligned} \tag{3.10}$$

where $A \neq B \neq C \neq A$, and the $\zeta$s are the same sign symbols. The corresponding active plastic potential functions are

$$\begin{aligned} G_1(\boldsymbol{\sigma}, \boldsymbol{\kappa}) &= \zeta_{AB}(\sigma_A - \sigma_B) - 2c\cos\psi + (\sigma_A + \sigma_B)\sin\psi, \\ G_2(\boldsymbol{\sigma}, \boldsymbol{\kappa}) &= \zeta_{AC}(\sigma_A - \sigma_C) - 2c\cos\psi + (\sigma_A + \sigma_C)\sin\psi. \end{aligned} \tag{3.11}$$

We introduce two non-negative discrete plastic multipliers, $\Delta\lambda_1$ and $\Delta\lambda_2$, and use Koiter's rule to obtain the plastic strain increment as

$$\Delta\epsilon_A^{\text{p}} = \Delta\lambda_1\frac{\partial G_1}{\partial \sigma_A} + \Delta\lambda_2\frac{\partial G_2}{\partial \sigma_A}, \tag{3.12}$$

where

$$\begin{aligned}\frac{\partial G_1}{\partial \sigma_I} &= \zeta_{AB}(\delta_{AI} - \delta_{BI}) + (\delta_{AI} + \delta_{BI})\sin\psi,\\ \frac{\partial G_2}{\partial \sigma_I} &= \zeta_{AC}(\delta_{AI} - \delta_{CI}) + (\delta_{AI} + \delta_{CI})\sin\psi.\end{aligned} \tag{3.13}$$

Letting $\Delta\lambda = \Delta\lambda_1 + \Delta\lambda_2$ and using the same hardening/softening law as for Case 1, we get

$$\begin{bmatrix}\chi_{11} & \chi_{12}\\ \chi_{21} & \chi_{22}\end{bmatrix}\begin{Bmatrix}\Delta\lambda_1\\ \Delta\lambda_2\end{Bmatrix} = \begin{Bmatrix}|\sigma_A^{\mathrm{tr}} - \sigma_B^{\mathrm{tr}}| - 2c_n\cos\phi + (\sigma_A^{\mathrm{tr}} + \sigma_B^{\mathrm{tr}})\sin\phi\\ |\sigma_A^{\mathrm{tr}} - \sigma_C^{\mathrm{tr}}| - 2c_n\cos\phi + (\sigma_A^{\mathrm{tr}} + \sigma_C^{\mathrm{tr}})\sin\phi\end{Bmatrix}, \tag{3.14}$$

where

$$\begin{aligned}\chi_{11} &= \chi_{22} = 4\mu + 4\lambda_{\mathrm{L}}\sin\phi\sin\psi + 4\mu\sin\phi\sin\psi + H,\\ \chi_{12} &= 4\lambda_{\mathrm{L}}\sin\phi\sin\psi + 2\mu(\zeta_{AB}\zeta_{AC} + \zeta_{AB}\sin\psi + \zeta_{AC}\sin\phi + \sin\phi\sin\psi) + H,\\ \chi_{21} &= 4\lambda_{\mathrm{L}}\sin\phi\sin\psi + 2\mu(\zeta_{AC}\zeta_{AB} + \zeta_{AC}\sin\psi + \zeta_{AB}\sin\phi + \sin\phi\sin\psi) + H.\end{aligned} \tag{3.15}$$

In the present case,

$$a_{AB} = a^{\mathrm{e}}_{AB} - \sum_{\alpha=1}^{2}\sum_{\beta=1}^{2}\sum_{I=1}^{3}\sum_{J=1}^{3}\chi^{\alpha\beta}a^{\mathrm{e}}_{AI}\frac{\partial G_\alpha}{\partial\sigma_I}\frac{\partial F_\beta}{\partial\sigma_J}a^{\mathrm{e}}_{JB}, \tag{3.16}$$

where $\chi^{\alpha\beta}$ is the $\alpha\beta$-component of the matrix inverse of $[\chi_{\alpha\beta}]$. In deciding whether one or two yield functions are active at a time, a search algorithm is required to identify the set of active constraints. For multisurface plasticity exhibiting corner-like effects a search algorithm for the set of active constraints is presented in [20] for the case of multiple linearly independent constraints, and in [21] for the case of multiple linearly dependent constraints. As noted in Section 1, these complications are avoided by considering smooth versions, which it was argued could be more accurate than the MC model.

### 3.2. A class of three-invariant plasticity models with smooth yield surfaces

Smooth yield functions are often substituted for the MC model to avoid the undesirable corner effects of the latter model, which are both tricky and unwieldy to implement. Consider then a family of smooth yield functions of the form

$$F(\boldsymbol{\sigma},\boldsymbol{\kappa}) = (k_1 I_3)^{1/3} - f(I_1, I_2) \leqslant 0, \quad k_1 = c_0 + \kappa_1\left(\frac{p_{\mathrm{a}}}{I_1}\right)^m, \tag{3.17}$$

where

$$I_1 = \sigma_1 + \sigma_2 + \sigma_3, \quad I_2 = \sigma_1\sigma_2 + \sigma_2\sigma_3 + \sigma_1\sigma_3, \quad I_3 = \sigma_1\sigma_2\sigma_3$$

are the first, second, and third stress invariants, respectively, $c_0$ and $m$ are model constants, $p_{\mathrm{a}} < 0$ is the atmospheric pressure expressed in the same units as $I_1$, and $\kappa_1 \in \boldsymbol{\kappa}$ is a plastic internal variable characterizing the friction hardening/softening of the material. A similar family of smooth plastic potential functions may be postulated as

$$G(\boldsymbol{\sigma},\boldsymbol{\kappa}) = (k_2 I_3)^{1/3} - g(I_1, I_2), \qquad k_2 = c_0 + \kappa_2\left(\frac{p_{\mathrm{a}}}{I_1}\right)^m, \tag{3.18}$$

where $\kappa_2 \in \boldsymbol{\kappa}$ characterizes the material's plastic dilatational response.

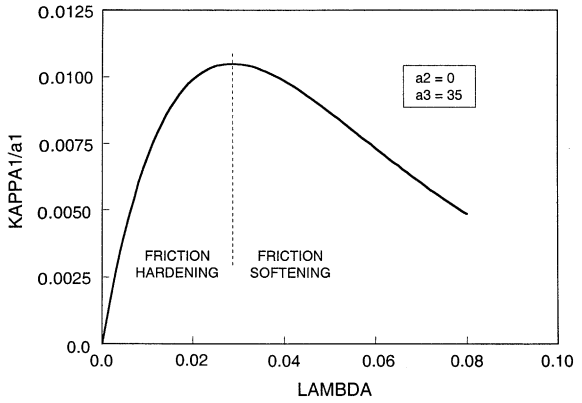


Fig. 2. Hardening/softening relation for parameter $\kappa_1$.

The hardening/softening law may be expressed in the form

$$\boldsymbol{\kappa} = \left\{ \begin{array}{c} \kappa_1 \\ \kappa_2 \end{array} \right\} = \boldsymbol{\kappa}(\boldsymbol{\sigma}, \lambda), \qquad \lambda = \int_t \dot{\lambda}\, \mathrm{d}t. \tag{3.19}$$

Here, $\kappa_1$ and $\kappa_2$ are non-negative functions. An example of a friction hardening/softening law is

$$\kappa_1(\boldsymbol{\sigma}, \lambda) = a_1 \lambda \exp(a_2 I_1) \exp(-a_3 \lambda), \tag{3.20}$$

where $a_1$, $a_2$, and $a_3$ are positive constants and $I_1 < 0$ is the first stress invariant. A typical plot of $\kappa_1$ as a function of the cumulative plastic strain $\lambda$ is shown in Fig. 2. The ascending part corresponds to friction hardening while the descending part suggests softening. The presence of the first stress invariant suggests that the growth of $\kappa_1$ decays with increasing confining pressure.

The class of plasticity models described above includes the following well-known three-invariant models widely used for characterizing the yield response of geomaterials such as concrete, soil and rock.

### *3.2.1. Lade–Duncan model*

The LD model [2] is recovered from (3.17) if we take

$$f(I_1, I_2) = I_1, \quad c_0 = 27, \quad m = 0. \tag{3.21}$$

In this case, plastic yielding takes place when $I_1^3/I_3 = k_1 \geqslant 27$, and $k_1 = c_0 + \kappa_1$. This model is widely used for characterizing the yield behavior of cohesionless granular materials such as sands under compressive normal stresses, i.e., $I_1 < 0$ and $I_3 < 0$. The yield function passes through the origin, implying no cohesive yield strength. The constant value $c_0 = 27$ arises from the constraint that the hydrostatic axis be contained by the yield function. With the hardening law given by (3.20), in which $\kappa_1$ increases from an initial value of zero when $\lambda = 0$, the initial yield function coincides with the hydrostatic axis. Thus, the initial elastic region reduces to a line. If some finite elastic region is to be represented before the beginning of a loading program, then $c_0$ must be chosen to be greater than 27.

Fig. 3 shows a cross section of the LD yield function on the deviatoric plane plotted on top of the hexagonal cross section of the MC yield function. The parameter $\kappa_1$ (or, equivalently, $k_1$) can be related analytically to the friction angle $\phi$ used in the MC plasticity model. For example, if the LD yield function is made to pass through the inner three tension corners of the MC hexagon, then (see Appendix A and [22])

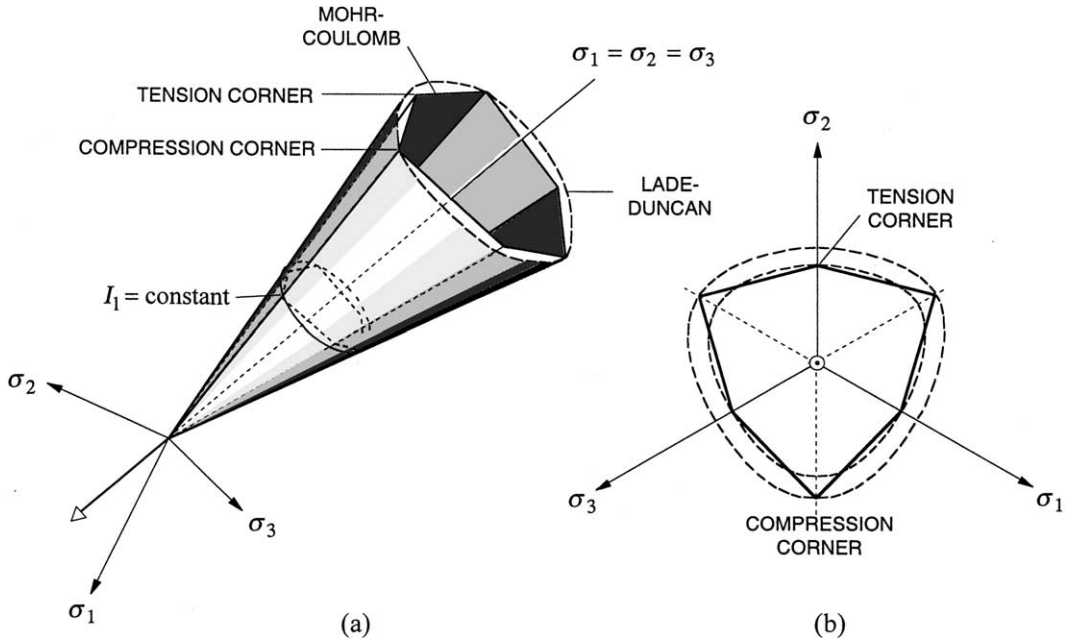


Fig. 3. LD and MC yield functions: (a) principal stress space representation; (b) deviatoric plane representation.

$$\frac{1}{3}\sin\phi_t = -\frac{a^2 - a + 1}{a^2 - 5a + 1}; \tag{3.22}$$

and if it is made to pass through the outer three compression corners, then

$$\frac{1}{3}\sin\phi_c = \frac{(a+1)^2 + \sqrt{3}(a^2-1)\mathrm{i}}{(a+1)^2 + 8a + \sqrt{3}(a^2-1)\mathrm{i}}, \tag{3.23}$$

where 'i' is the imaginary number, and

$$a = \left(\frac{\kappa_1 - 27 + 6\sqrt{3\kappa_1}\mathrm{i}}{\kappa_1 + 27}\right)^{1/3}. \tag{3.24}$$

Note in the above equations that $a$ has an imaginary part but the right-hand sides of (3.22) and (3.23) are both real numbers. The variations of $\phi_t$ and $\phi_c$ with $\kappa_1$ are shown in Fig. 4.

### 3.2.2. Modified Lade model

The modified Lade (ML) model [7] is obtained if we take

$$f(I_1, I_2) = I_1, \quad c_0 = 27, \quad 0 < m < 1. \tag{3.25}$$

The presence of the exponential term $(p_a/I_1)^m$ makes the yield function curve parallel to the hydrostatic axis with increasing confining pressure. The LD model is a special case of the ML model when $m = 0$.

The relationships between $\phi_t$, $\phi_c$, and the ML model parameters can be obtained by taking

$$\kappa_0 = \kappa_1\left(\frac{p_a}{I_1}\right)^m \tag{3.26}$$

and substituting $\kappa_0$ in lieu of $\kappa_1$ in (3.24). Note that $\kappa_0 = \kappa_1$ if $m = 0$. If $m > 0$, then $\kappa_0 \to 0$ as $I_1 \to -\infty$. In this case,

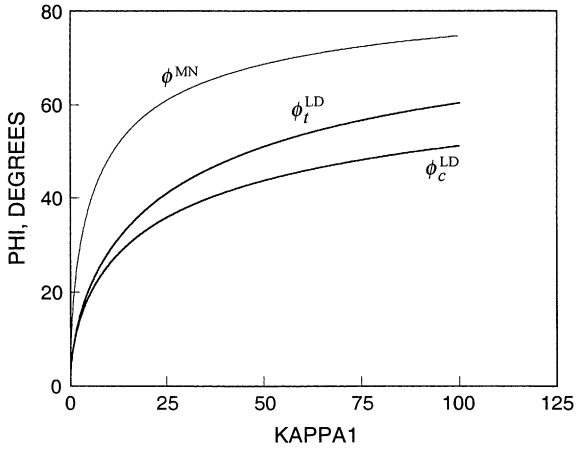


Fig. 4. Relation among LD parameter $\kappa_1$, MN parameter $\kappa_1$, and MC friction angle parameter $\phi$.

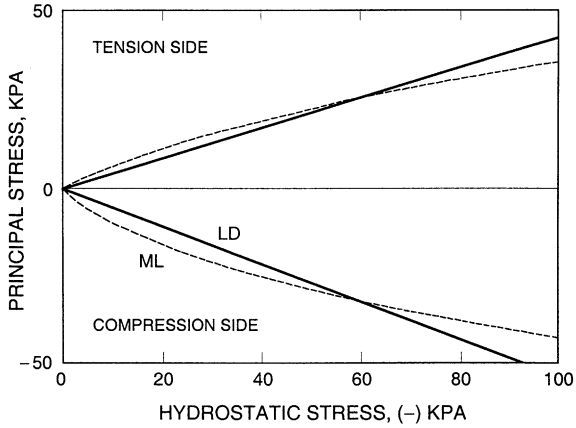


Fig. 5. LD and ML yield surfaces on meridian plane.

$$\lim_{I_1\to-\infty} a = (-1)^{1/3} = \frac{1}{2} + \frac{\sqrt{3}}{2}\mathrm{i}, \tag{3.27}$$

and so, from (3.22) and (3.23), we get

$$\lim_{I_1\to-\infty} \sin\phi_{\mathrm{t}} = \lim_{I_1\to-\infty} \sin\phi_{\mathrm{c}} = 0. \tag{3.28}$$

Thus, the equivalent friction angle is such that the MC yield surface also curves parallel to the hydrostatic axis with increasing confining pressures. A plot of the ML model on a meridian plane is shown in Fig. 5, along with a plot of the LD model (with $p_{\mathrm{a}} = -100$ kPa, $m = 1$ and $\kappa_1 = 13$).

### *3.2.3. Matsuoka–Nakai model*

The MN model [3] is obtained if we take

$$f(I_1, I_3) = (I_1 I_2)^{1/3}, \quad c_0 = 9, \quad m = 0. \tag{3.29}$$

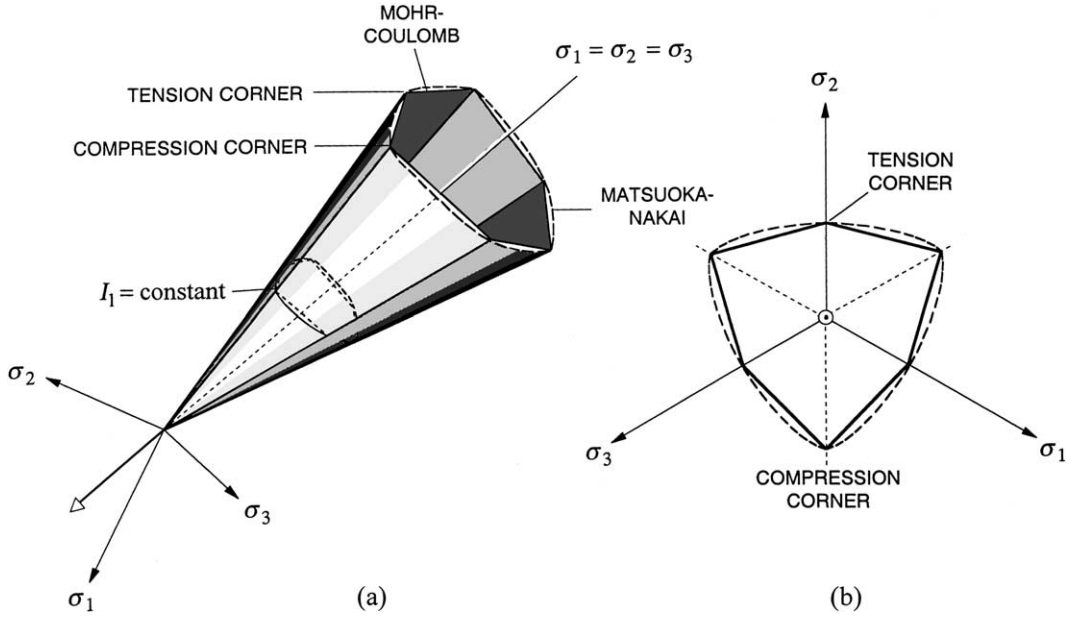


Fig. 6. MN and MC yield functions: (a) principal stress space representation; (b) deviatoric plane representation.

In this case, yielding takes place when $I_1 I_2 / I_3 = k_1$. The constant $c_0 = 9$ ensures that the hydrostatic axis is contained in the yield function $F$. If $\kappa_1 = 0$ when $\lambda = 0$, then the initial yield function coincides with the hydrostatic axis. The cross section of the MN model on the deviatoric plane is plotted in Fig. 6 together with the MC yield surface. Note in this case that the MN yield surface passes through all six corners of the MC hexagon.

It is possible to relate the parameter $k_1$ of the MN model with the friction angle $\phi$ of the MC model. Here, the relationship between the two parameters is unique since there is only one function of the form (3.26) that passes through all six corners of the irregular hexagon. The relationship is (see Appendix A and [22])

$$\sin\phi = \left(\frac{k_1 - 9}{k_1 - 1}\right)^{1/2} = \left(\frac{\kappa_1}{\kappa_1 + 8}\right)^{1/2}. \tag{3.30}$$

As $\kappa_1$ increases from an initial value of zero when the yield function coincides with the hydrostatic axis, the equivalent friction angle also increases (friction hardening); conversely, as $\kappa_1$ decreases from its peak value according to the hardening/softening law (3.20), the equivalent friction angle also decreases (friction softening). The variation of $\phi$ with $\kappa_1$ is also shown in Fig. 4.

The generalized yield function defined by (3.17) allows the extension of the MN model to the case where the yield function may also curve parallel to the hydrostatic axis with increasing confining pressure, as in the ML model. Furthermore, in principle the functions $f(I_1, I_2)$ and $g(I_1, I_2)$ do not necessarily have to be the same, so a LD yield function, for example, may be combined with a MN plastic potential function, and vice versa, depending on the desired model features. Several other three-invariant isotropic yield functions have been analyzed in [1], with the consensus that the LD and MN models ensure convexity of the yield surfaces while the other forms considered by previous investigators may not. Without loss of generality this paper will thus focus on the numerical implementation of the family of smooth yield functions given by (3.17).

### 3.3. Return mapping algorithm in principal stress axes

For the three-invariant plasticity models of the form described in Section 3.2, we adopt the following standard return mapping algorithm in principal stress space:

$$\sigma_A = \sigma_A^{\mathrm{tr}} - \Delta\lambda \sum_{B=1}^{3} a_{AB}^{\mathrm{e}} \frac{\partial G}{\partial \sigma_B}, \tag{3.31}$$

where $\Delta\lambda > 0$ is a discrete plastic multiplier. A rewrite of this equation in principal elastic strain space is

$$\epsilon_A^{\mathrm{e}} - \epsilon_A^{\mathrm{e\,tr}} + \Delta\lambda \frac{\partial G}{\partial \sigma_A} = 0, \tag{3.32}$$

where

$$\epsilon_A^{\mathrm{e}} = \sum_{B=1}^{3} a_{AB}^{\mathrm{e}-1} \sigma_B, \qquad \epsilon_A^{\mathrm{e\,tr}} = \sum_{B=1}^{3} a_{AB}^{\mathrm{e}-1} \sigma_B^{\mathrm{tr}} \tag{3.33}$$

and

$$[a_{AB}^{\mathrm{e}}]^{-1} = \frac{1}{E} \begin{bmatrix} 1 & -\nu & -\nu \\ -\nu & 1 & -\nu \\ -\nu & -\nu & 1 \end{bmatrix} \tag{3.34}$$

is the elastic compliance matrix that depends on the elastic Young's modulus $E$ and Poisson's ratio $\nu$. Although the stress form return-mapping algorithm (3.31) is more commonly used in practice, the strain form (3.32) is more robust since it can handle non-linear elasticity as well. For isotropic linear elasticity the two forms are the same from an implementational standpoint.

We also assume an evolution equation for the internal plastic variables of the form

$$\boldsymbol{\kappa} - \hat{\boldsymbol{\kappa}}(\boldsymbol{\beta}, \lambda) = \mathbf{0}, \qquad \lambda = \lambda_n + \Delta\lambda, \tag{3.35}$$

where $\hat{\boldsymbol{\kappa}}$ is some prescribed hardening/softening law such as that given by the exponential function (3.20), and $\boldsymbol{\beta} = \{\sigma_1, \sigma_2, \sigma_3\}$ is the vector of principal Cauchy stresses. The above hardening/softening law states that friction hardening/softening may also depend on the stress state. This latter feature is consistent with the experimental observations described in [23], for example, where the rate of friction hardening/softening was shown to be influenced by the value of the first stress invariant as well. For a plastic loading process, we write the discrete consistency condition as

$$F(\boldsymbol{\beta}, \boldsymbol{\kappa}) = 0, \tag{3.36}$$

where $F$ is the yield function.

In a strain-driven problem we are generally given a fixed set of predictor values $\sigma_A^{\mathrm{tr}}$ (or $\epsilon_A^{\mathrm{e\,tr}}$), for $A = 1, 2, 3$, and the goal is to find the corresponding values of $\boldsymbol{\beta}$, $\boldsymbol{\kappa}$, and $\Delta\lambda$ satisfying (3.31), (3.35) and (3.36). We can readily solve the non-linear problem using a standard Newton iteration, defining the vector of unknowns and the local tangent operator as

$$\boldsymbol{x} = \begin{Bmatrix} \boldsymbol{\beta} \\ \boldsymbol{\kappa} \\ \Delta\lambda \end{Bmatrix}, \qquad \boldsymbol{A} = \boldsymbol{r}'(\boldsymbol{x}) = \begin{bmatrix} (\boldsymbol{a}^{\mathrm{e}-1} + \Delta\lambda G_{,\boldsymbol{\beta}\boldsymbol{\beta}}) & \Delta\lambda G_{,\boldsymbol{\beta}\boldsymbol{\kappa}} & G_{,\boldsymbol{\beta}} \\ -\hat{\boldsymbol{\kappa}}_{,\boldsymbol{\beta}} & \boldsymbol{I}_{n_\kappa \times n_\kappa} & -\hat{\boldsymbol{\kappa}}_{,\lambda} \\ F_{,\boldsymbol{\beta}} & F_{,\boldsymbol{\kappa}} & 0 \end{bmatrix}, \tag{3.37}$$

where $\boldsymbol{r}$ is the residual vector and $\boldsymbol{I}_{n_\kappa \times n_\kappa}$ is an identity matrix of dimension $n_\kappa$, the dimension of the vector $\boldsymbol{\kappa}$. The same local tangent operator $\boldsymbol{A}$ may be used to define the consistent tangent operator for the global

iteration. In this case, the material tangent operator $\boldsymbol{a}$, with components $a_{AB} = \partial\sigma_A/\partial\epsilon_B$, may be obtained from the tangent operator $\boldsymbol{A}$ as (see [24])

$$\boldsymbol{a} = [\boldsymbol{I}_{3\times 3}|\boldsymbol{0}] \cdot \boldsymbol{A}^{-1} \cdot \begin{bmatrix} \boldsymbol{I}_{3\times 3} \\ \hline \boldsymbol{0} \end{bmatrix}. \tag{3.38}$$

From a numerical standpoint, all that is necessary is to invert $\boldsymbol{A}$, and the first $3 \times 3$ submatrix of $\boldsymbol{A}^{-1}$ defines the matrix $\boldsymbol{a}$, which in turn is used in the complete tangent operator $\mathbf{c}$ via (2.12).

### 3.4. Derivatives

Consider the following relationship between the dilatancy parameter $\kappa_2$ and the friction parameter $\kappa_1$:

$$\kappa_2 = \alpha\kappa_1, \quad \alpha \in [0, 1]. \tag{3.39}$$

Here, $\alpha \neq 1$ corresponds to the case of non-associative plasticity. For sands a value of $\alpha < 1$ is typical [7]. Because we have now adopted an explicit relation between $\kappa_1$ and $\kappa_2$, the total number of unknowns can be reduced in the local Newton iteration problem. Eliminating the variable $\kappa_2$ from the original set of unknowns, we can re-write

$$\boldsymbol{x} = \begin{Bmatrix} \boldsymbol{\beta} \\ \kappa_1 \\ \Delta\lambda \end{Bmatrix}_{5\times 1}, \qquad \boldsymbol{r}(\boldsymbol{x}) = \begin{Bmatrix} \epsilon_A^{\mathrm{e}} - \epsilon_A^{\mathrm{e\,tr}} + \Delta\lambda\,\partial G/\partial\sigma_A \\ \kappa_1 - \hat{\kappa}_1(\sigma_1, \sigma_2, \sigma_3, \lambda) \\ F(\sigma_1, \sigma_2, \sigma_3, \kappa_1) \end{Bmatrix}_{5\times 1}, \tag{3.40}$$

where $A = 1, 2, 3$; $\boldsymbol{\beta}$ is the vector of principal Cauchy stresses; and $\epsilon_A^{\mathrm{e}}$ and $\epsilon_A^{\mathrm{e\,tr}}$ are defined by (3.33) as linear functions of $\boldsymbol{\beta}$ and $\boldsymbol{\beta}^{\mathrm{tr}}$, respectively. In this case the local tangent operator simplifies to

$$\boldsymbol{A} = \boldsymbol{r}'(\boldsymbol{x}) = \begin{bmatrix} (\boldsymbol{a}^{\mathrm{e}-1} + \Delta\lambda\, G_{,\boldsymbol{\beta}\boldsymbol{\beta}}) & \alpha\Delta\lambda\, G_{,\boldsymbol{\beta}\kappa_2} & G_{,\boldsymbol{\beta}} \\ -\hat{\kappa}_{1,\boldsymbol{\beta}} & 1 & -\hat{\kappa}_{1,\lambda} \\ F_{,\boldsymbol{\beta}} & F_{,\kappa_1} & 0 \end{bmatrix}_{5\times 5}. \tag{3.41}$$

The inverse $\boldsymbol{A}^{-1}$ may be calculated readily from the IMSL subroutines LSGRR/DLSGRR.

The derivatives of the yield and plastic potential functions are given, respectively, by

$$\begin{aligned} \frac{\partial F}{\partial\sigma_A} &= \frac{1}{3\sigma_A}(k_1 I_3)^{1/3} - \frac{1}{3} b_1 k_1^{-2/3} - \frac{\partial f}{\partial\sigma_A}, \\ \frac{\partial G}{\partial\sigma_A} &= \frac{1}{3\sigma_A}(k_2 I_3)^{1/3} - \frac{1}{3} b_2 k_2^{-2/3} - \frac{\partial g}{\partial\sigma_A}, \end{aligned} \tag{3.42}$$

where

$$k_1 = c_0 + \kappa_1 \left(\frac{p_{\mathrm{a}}}{I_1}\right)^m, \qquad k_2 = c_0 + \kappa_2 \left(\frac{p_{\mathrm{a}}}{I_1}\right)^m; \tag{3.43}$$

$$b_1 = m\kappa_1 \left(\frac{p_{\mathrm{a}}}{I_1}\right)^m \frac{I_3^{1/3}}{I_1}, \qquad b_2 = m\kappa_2 \left(\frac{p_{\mathrm{a}}}{I_1}\right)^m \frac{I_3^{1/3}}{I_1}; \tag{3.44}$$

and

$$\frac{\partial f}{\partial\sigma_A} = \frac{\partial g}{\partial\sigma_A} = \begin{cases} 1, & \text{for LD;} \\ [I_1(I_1 - \sigma_A) + I_2]/[3(I_1 I_2)^{2/3}], & \text{for MN.} \end{cases} \tag{3.45}$$

For the second stress derivative of the plastic potential function we have

$$\frac{\partial^2 G}{\partial\sigma_A\,\partial\sigma_B}=\frac{1}{3}(k_2 I_3)^{1/3}\left(\frac{1}{3\sigma_A\sigma_B}-\frac{\delta_{AB}}{\sigma_A^2}\right)+\frac{k_2^{-2/3}}{9}\left(\frac{I_3^{1/3}}{\sigma_A}+2\frac{b_2}{k_2}\right)\frac{\partial k_2}{\partial\sigma_B}-\frac{1}{3}k_2^{-2/3}\frac{\partial b_2}{\partial\sigma_B}-\frac{\partial^2 g}{\partial\sigma_A\,\partial\sigma_B}, \tag{3.46}$$

where

$$\frac{\partial k_2}{\partial\sigma_B}=-\frac{m\kappa_2}{I_1}\left(\frac{p_a}{I_1}\right)^m,\qquad \frac{\partial b_2}{\partial\sigma_B}=\frac{b_2}{I_1}\left(\frac{I_1}{3\sigma_B}-m-1\right), \tag{3.47}$$

$\partial^2 g/\partial\sigma_A\,\partial\sigma_B=0$ for the LD model, and

$$\frac{\partial^2 g}{\partial\sigma_A\,\partial\sigma_B}=\frac{1}{3}(I_1 I_2)^{-2/3}(3I_1-\sigma_A-\sigma_B-I_1\delta_{AB})-\frac{2}{9}(I_1 I_2)^{-5/3}[I_1(I_1-\sigma_A)+I_2][I_1(I_1-\sigma_B)+I_2] \tag{3.48}$$

for the MN model.

Finally, we have

$$\frac{\partial^2 G}{\partial\sigma_A\,\partial\kappa_2}=\frac{1}{3}k_2^{-2/3}\left(\frac{p_a}{I_1}\right)^m\left(\frac{1}{3}\frac{I_3^{1/3}}{\sigma_A}+\frac{2}{3}\frac{b_2}{k_2}-m\frac{I_3^{1/3}}{I_1}\right) \tag{3.49}$$

and

$$\frac{\partial F}{\partial\kappa_1}=\frac{1}{3}k_1^{-2/3}I_3^{1/3}\left(\frac{p_a}{I_1}\right)^m. \tag{3.50}$$

Assuming an exponential form (3.20) for the plastic internal variable $\kappa_1$, we also get

$$\frac{\partial\hat{\kappa}_1}{\partial\sigma_A}=a_1 a_2\lambda\exp(a_2 I_1)\exp(-a_3\lambda) \tag{3.51}$$

and

$$\frac{\partial\hat{\kappa}_1}{\partial\lambda}=(1-a_3\lambda)a_1\exp(a_2 I_1)\exp(-a_3\lambda), \tag{3.52}$$

where a 'hat' over $\kappa_1$ is used to distinguish the function under consideration from the variable $\kappa_1$ itself, which is now treated as one of the unknowns.

## 4. Extension to finite deformation plasticity

As noted in Section 1, the notion of return mapping in principal stress space was developed initially to address the problem of geometric non-linearity and not the complexity of the constitutive model. Thus, an 'extension' to the finite deformation regime of the proposed algorithmic framework is straightforward (strictly speaking, the proposed approach has been extended to the infinitesimal case, hence, the in quotes). In this section we briefly review the structure of the finite deformation theory and present two alternative methods of constructing the algorithmic tangent operator applicable to the three-invariant constitutive formulation.

### *4.1. Variational equation*

Once again, our point of departure is the variational form of the linear momentum balance, now written with respect to the reference configuration as

$$\mathscr{W} = \int_{\mathscr{B}} (\mathrm{GRAD}\,\boldsymbol{\eta} : \boldsymbol{P} - \rho_0 \boldsymbol{\eta} \cdot \mathbf{G})\,\mathrm{d}V - \int_{\partial\mathscr{B}} \boldsymbol{\eta} \cdot \boldsymbol{t}_0\,\mathrm{d}A = 0, \tag{4.1}$$

where $\boldsymbol{P}$ is the unsymmetric first Piola–Kirchhoff stress tensor, $\rho_0$ is the mass density in the reference configuration, $\mathbf{G}$ is the vector of gravity accelerations, $\boldsymbol{t}_0$ is the nominal traction vector, $\boldsymbol{\eta}$ is the weighting function, and $\mathscr{B}$ and $\partial\mathscr{B}$ are, respectively, the problem domain and boundary in the reference configuration. The gradient operator GRAD is a spatial differentiation with respect to the coordinates of the reference configuration. We note that the stress tensor $\boldsymbol{P}$ is related to the symmetric Kirchhoff stress tensor $\boldsymbol{\tau}$ through the deformation gradient $\boldsymbol{F} = \partial\boldsymbol{\phi}/\partial\boldsymbol{X}$ via the relation $\boldsymbol{\tau} = \boldsymbol{P} \cdot \boldsymbol{F}^{\mathrm{t}}$, and thus we can make the following substitution in (4.1):

$$\mathrm{GRAD}\,\boldsymbol{\eta} : \boldsymbol{P} \equiv \mathrm{grad}\,\boldsymbol{\eta} : \boldsymbol{\tau}, \tag{4.2}$$

where grad is a spatial differentiation with respect to the coordinates of the current configuration.

For dead loading the linearization of (4.1) with respect to the state $\mathscr{W}^0$ reads

$$L\mathscr{W} = \mathscr{W}^0 + \int_{\mathscr{B}} \mathrm{grad}\,\boldsymbol{\eta} : \delta\boldsymbol{\tau}\,\mathrm{d}V + \int_{\mathscr{B}} \delta(\mathrm{grad}\,\boldsymbol{\eta}) : \boldsymbol{\tau}\,\mathrm{d}V - \int_{\partial\mathscr{B}} \boldsymbol{\eta} \cdot \delta\boldsymbol{t}_0\,\mathrm{d}A. \tag{4.3}$$

In terms of the variation of the displacement field $\delta\boldsymbol{u}$, we herein write the tangential constitutive equation as

$$\delta\boldsymbol{\tau} = \boldsymbol{\alpha} : \mathrm{grad}\,\delta\boldsymbol{u}, \tag{4.4}$$

where $\boldsymbol{\alpha}$ is a fourth-order tangent constitutive operator that may also include some stress terms. The variation of the second term in the integrals of (4.3) takes the form

$$\delta(\mathrm{grad}\,\boldsymbol{\eta}) = \delta(\mathrm{GRAD}\,\boldsymbol{\eta} \cdot \boldsymbol{F}^{-1}) = \mathrm{GRAD}\,\boldsymbol{\eta} \cdot \delta\boldsymbol{F}^{-1} = -\mathrm{grad}\,\boldsymbol{\eta} \cdot \mathrm{grad}\,\delta\boldsymbol{u}. \tag{4.5}$$

Thus, Eq. (4.3) can be rewritten as

$$L\mathscr{W} = \mathscr{W}^0 + \int_{\mathscr{B}} \mathrm{grad}\,\boldsymbol{\eta} : \mathbf{a} : \mathrm{grad}\,\delta\boldsymbol{u}\,\mathrm{d}V - \int_{\partial\mathscr{B}} \boldsymbol{\eta} \cdot \delta\boldsymbol{t}_0\,\mathrm{d}A, \tag{4.6}$$

where

$$\mathbf{a} = \boldsymbol{\alpha} - \boldsymbol{\tau} \ominus \mathbf{1} \tag{4.7}$$

and $(\boldsymbol{\tau} \ominus \mathbf{1})_{ijkl} = \tau_{il}\delta_{jk}$. This expression is valid provided that an incremental constitutive relation of the form (4.4) is available.

### 4.2. Tangent operators for multiplicative plasticity

We are specifically interested in the form of the tangent constitutive tensor $\boldsymbol{\alpha}$ arising from the product formula algorithm of multiplicative plasticity as presented in [8,9]. In the interest of brevity, details of the formulation of the multiplicative plasticity theory will not be repeated here—we simply refer the readers to [8,9], and to Box 2, which summarizes the important steps of the algorithm. Our goal is to compare two alternative approaches for constructing the tangent operator $\boldsymbol{\alpha}$. To this end, we again resort to the proposed spectral decomposition technique.

First, we write the Kirchhoff stress tensor spectrally as

$$\boldsymbol{\tau} = \sum_{A=1}^{3} \tau_A \boldsymbol{m}^{(A)}, \quad \boldsymbol{m}^{(A)} = \boldsymbol{n}^{(A)} \otimes \boldsymbol{n}^{(A)}, \tag{4.8}$$

Box 2. Return mapping algorithm in principal stress axes for isotropically hardening three-invariant plasticity model, finite deformation case

Step 1. Compute $\boldsymbol{b}^{\mathrm{e\,tr}} = \boldsymbol{f} \cdot \boldsymbol{b}^{\mathrm{e}}_n \cdot \boldsymbol{f}^{\mathrm{t}}$
Step 2. Spectrally decompose $\boldsymbol{b}^{\mathrm{e\,tr}} = \sum_{A=1}^{3} b_A \boldsymbol{m}^{\mathrm{tr}(A)}$
Step 3. Compute $\tau_A^{\mathrm{tr}} = \sum_{B=1}^{3} a^{\mathrm{e}}_{AB} \varepsilon_B$ for $A = 1, 2, 3$
Step 4. Check $F(\tau_1^{\mathrm{tr}}, \tau_2^{\mathrm{tr}}, \tau_3^{\mathrm{tr}}, \boldsymbol{\kappa}_n) > 0$? No, set $\boldsymbol{\tau} = \sum_{A=1}^{3} \tau_A^{\mathrm{tr}} \boldsymbol{m}^{\mathrm{tr}(A)}$ and exit.
Step 5. Yes, solve $F(\Delta\lambda) = 0$ for $\Delta\lambda$
Step 6. Compute $\tau_A = \tau_A^{\mathrm{tr}} - \Delta\lambda \sum_{B=1}^{3} a^{\mathrm{e}}_{AB} \partial G / \partial \tau_B$
Step 7. Update $\boldsymbol{\tau} = \sum_{A=1}^{3} \tau_A \boldsymbol{m}^{\mathrm{tr}(A)}$, $\boldsymbol{\kappa} = \boldsymbol{\kappa}_n + \Delta\boldsymbol{\kappa}$ and exit.

where $\tau_A$ and $\boldsymbol{n}^{(A)}$ are the eigenvalues and unit eigendirections of $\boldsymbol{\tau}$, respectively. We view the constitutive variation of $\boldsymbol{\tau}$ as being driven by the elastic left Cauchy–Green deformation tensor $\boldsymbol{b}^{\mathrm{e}}$, whose predictor value is given by

$$\boldsymbol{b}^{\mathrm{e\,tr}} = \boldsymbol{f} \cdot \boldsymbol{b}^{\mathrm{e}}_n \cdot \boldsymbol{f}^{\mathrm{t}}, \quad \boldsymbol{f} = \frac{\partial \boldsymbol{x}}{\partial \boldsymbol{x}_n}, \tag{4.9}$$

where $\boldsymbol{b}^{\mathrm{e}}_n$ is the converged value of $\boldsymbol{b}^{\mathrm{e}}$ at the configuration $\phi(\mathscr{B}, t_n)$. By isotropy in the elastic response, we can also decompose $\boldsymbol{b}^{\mathrm{e\,tr}}$ spectrally as

$$\boldsymbol{b}^{\mathrm{e\,tr}} = \sum_{A=1}^{3} b_A \boldsymbol{m}^{(A)}, \tag{4.10}$$

where $b_A = \lambda_A^2$ are the squares of the trial elastic principal stretches $\lambda_A$, and $\boldsymbol{m}^{(A)}$ are the same spectral directions as those of the stress tensor $\boldsymbol{\tau}$. The variation of $\tau_A$ with respect to the principal value $b_B$ of the deformation tensor $\boldsymbol{b}^{\mathrm{e\,tr}}$ is linked by the chain rule through the intermediate variable $\varepsilon_B := \ln \lambda_B$, the principal elastic logarithmic strain. Thus, in a deformation-driven format return-mapping may be viewed as taking place in the principal Kirchhoff stress space according to prescribed predictor values of the principal elastic logarithmic strains [8,9].

*4.2.1. Form 1. Tangent operator constructed from eigenbases*

As before, the tangent operator $\boldsymbol{\alpha}$ is obtained by direct differentiation of the spectrally decomposed Kichhoff stress tensor (cf. (2.13)),

$$\boldsymbol{\alpha} = \sum_{A=1}^{3} \sum_{B=1}^{3} a_{AB} \boldsymbol{m}^{(A)} \otimes \boldsymbol{m}^{(B)} + \sum_{A=1}^{3} \tau_A \boldsymbol{\omega}^{(A)}, \tag{4.11}$$

where $a_{AB} = \partial \tau_A / \partial \varepsilon_B$ is the tangent operator consistent with the return mapping in principal Kirchhoff stress directions, and where $\varepsilon_B = \ln \lambda_B$ and $\lambda_B^2 = b_B$. The tensor $\boldsymbol{\omega}^{(A)}$ reflects the changing orientation of the spectral directions of $\boldsymbol{\tau}$ (or $\boldsymbol{b}^{\mathrm{e\,tr}}$) and takes the form [8]

$$\begin{aligned} \boldsymbol{\omega}^{(A)} = 2[&\boldsymbol{I}_b - \boldsymbol{b} \otimes \boldsymbol{b} + I_3 b_A^{-2} (\mathbf{1} \otimes \mathbf{1} - \boldsymbol{I}) + b_A^2 (\boldsymbol{b} \otimes \boldsymbol{m}^{(A)} + \boldsymbol{m}^{(A)} \otimes \boldsymbol{b}) \\ &- I_3 b_A^{-2} (\mathbf{1} \otimes \boldsymbol{m}^{(A)} + \boldsymbol{m}^{(A)} \otimes \mathbf{1}) - \psi \boldsymbol{m}^{(A)} \otimes \boldsymbol{m}^{(A)}] / D_A, \end{aligned} \tag{4.12}$$

where $\boldsymbol{b} := \boldsymbol{b}^{\mathrm{e\,tr}}$, $I_1$ and $I_3$ are the first and third invariants of $\boldsymbol{b}$,

$$\boldsymbol{I}_b = (\boldsymbol{b} \oplus \boldsymbol{b} + \boldsymbol{b} \ominus \boldsymbol{b})/2, \qquad \psi = I_1 + I_3 b_A^{-2} - 4 b_A \tag{4.13}$$

and

$$D_A := 2b_A^2 - I_1 b_A + I_3 b_A^{-1} 0. \tag{4.14}$$

To derive the tangential spin $\boldsymbol{\omega}^{(A)}$ we note once again that it only suffices to know the eigenvalues $b_A$ and eigenbases $\boldsymbol{m}^{(A)}$, but not the eigenvectors $\boldsymbol{n}^{(A)}$ of the original tensor $\boldsymbol{b}^{\mathrm{e\,tr}}$. As noted in Section 2, closed form solutions for these eigenvalues and eigenbases are available. The above form for the tangent operator $\boldsymbol{\alpha}$ is widely used in the computational mechanics literature although it arguably requires more detailed numerical calculations than the one described below.

*4.2.2. Form 2. Tangent operator constructed from eigenvectors*

Following Ogden's [11] formulation, we write the variation of the Kirchhoff stress tensor as

$$\delta\boldsymbol{\tau} = \sum_{A=1}^{3} \delta\tau_A \boldsymbol{m}^{(A)} + \sum_{A=1}^{3} \sum_{B\neq A} \Omega_{AB}(\tau_B - \tau_A)\boldsymbol{m}^{(AB)}, \tag{4.15}$$

where $\Omega_{AB}$ is the spin of the principal axes of $\boldsymbol{\tau}$, and $\boldsymbol{m}^{(AB)} = \boldsymbol{n}^{(A)} \otimes \boldsymbol{n}^{(B)}$. The variation of $\boldsymbol{b}^{\mathrm{e\,tr}}$ takes a similar form,

$$\delta\boldsymbol{b}^{\mathrm{e\,tr}} = \sum_{A=1}^{3} \delta b_A \boldsymbol{m}^{(A)} + \sum_{A=1}^{3} \sum_{B\neq A} \Omega_{AB}(b_B - b_A)\boldsymbol{m}^{(AB)}. \tag{4.16}$$

Note that the spins of the principal axes of $\boldsymbol{\tau}$ and $\boldsymbol{b}^{\mathrm{e\,tr}}$ are the same because of the assumed isotropy in the elastic response. It thus follows that

$$\delta\boldsymbol{\tau} = \boldsymbol{\varphi} : \delta\boldsymbol{b}^{\mathrm{e\,tr}}, \tag{4.17}$$

where $\boldsymbol{\varphi} := \partial\boldsymbol{\tau}/\partial\boldsymbol{b}^{\mathrm{e\,tr}}$ is a rank-four tangential stress-deformation tensor of the form

$$\boldsymbol{\varphi} = \sum_{A=1}^{3} \sum_{B=1}^{3} \frac{\partial\tau_A}{\partial b_B} \boldsymbol{m}^{(A)} \otimes \boldsymbol{m}^{(B)} + \frac{1}{2} \sum_{A=1}^{3} \sum_{B\neq A} \left( \frac{\tau_B - \tau_A}{b_B - b_A} \right) \left( \boldsymbol{m}^{(AB)} \otimes \boldsymbol{m}^{(AB)} + \boldsymbol{m}^{(AB)} \otimes \boldsymbol{m}^{(BA)} \right). \tag{4.18}$$

We note from the equation above that the spins $\Omega_{AB}$ do not enter into the expression for the tensor $\boldsymbol{\varphi}$.

From (4.9), we obtain the variation

$$\delta\boldsymbol{b}^{\mathrm{e\,tr}} = \delta\boldsymbol{f} \cdot \boldsymbol{b}_n^{\mathrm{e}} \cdot \boldsymbol{f}^{\mathrm{t}} + \boldsymbol{f} \cdot \boldsymbol{b}_n^{\mathrm{e}} \cdot \delta\boldsymbol{f}^{\mathrm{t}} = \operatorname{grad}\delta\boldsymbol{u} \cdot \boldsymbol{b}^{\mathrm{e\,tr}} + \boldsymbol{b}^{\mathrm{e\,tr}} \cdot \operatorname{grad}^{\mathrm{t}}\delta\boldsymbol{u}. \tag{4.19}$$

On substitution into (4.17), we get

$$\delta\boldsymbol{\tau} = 2\boldsymbol{\varphi} \cdot \boldsymbol{b}^{\mathrm{e\,tr}} : \operatorname{grad}\delta\boldsymbol{u} \equiv \boldsymbol{\alpha} : \operatorname{grad}\delta\boldsymbol{u}, \tag{4.20}$$

where

$$\boldsymbol{\alpha} = 2\boldsymbol{\varphi} \cdot \boldsymbol{b}^{\mathrm{e\,tr}} = 2\boldsymbol{\varphi} \cdot \sum_{C=1}^{3} b_C \boldsymbol{m}^{(C)}. \tag{4.21}$$

Noting that

$$\frac{\partial\tau_A}{\partial b_B} = \frac{\partial\tau_A}{\partial\varepsilon_B} \frac{\partial\varepsilon_B}{\partial\lambda_B} \frac{\partial\lambda_B}{\partial b_B} = \frac{a_{AB}}{2b_B}, \tag{4.22}$$

where $a_{AB} = \partial\tau_A/\partial\varepsilon_B$, we finally have

$$\boldsymbol{\alpha} = \sum_{A=1}^{3} \sum_{B=1}^{3} a_{AB} \boldsymbol{m}^{(A)} \otimes \boldsymbol{m}^{(B)} + \frac{1}{2} \sum_{A=1}^{3} \sum_{B\neq A} \left( \frac{\tau_B - \tau_A}{b_B - b_A} \right) (b_B \boldsymbol{m}^{(AB)} \otimes \boldsymbol{m}^{(AB)} + b_A \boldsymbol{m}^{(AB)} \otimes \boldsymbol{m}^{(BA)}). \tag{4.23}$$

This tangent operator must be compared to (4.11), which exhibits a very similar structure. The first term of (4.23) is identical to that of (4.11) and reflects the return mapping algorithm in principal Kirchhoff stress space. The second term reflects the spin of the spectral directions and appears to have a much simpler structure than the spin components defined in (4.12), although the spin components of (4.23) do require explicit evaluation of the eigenvectors. The latter feature should not be viewed as a shortcoming since, as noted in the previous section, there exist iterative solvers that calculate the eigenvalues and eigenvectors of a symmetric second-order tensor efficiently. Besides, the spin component of (4.23) is a relatively simple expression that is very easy to code. An example presented in the next section demonstrates that the two alternative tangent operators described above are the same.

## 5. Numerical examples

In this section we present the results of a number of two- and three-dimensional element tests as well as a full boundary-value problem analysis reporting the performance of the proposed algorithm. In the analyses we assess the ability of the algorithm to handle (a) the degree of material non-linearity implied by the smooth three-invariant model, (b) the rotation of principal stress axes, and (c) the finite deformation effects.

### *5.1. Element tests: simulations with smooth three-invariant models*

In the following examples we discuss the implementation of two smooth versions of the MC model—the ML model and the MN model discussed in Section 3.2. For the ML model with $c_0 = 27$, we assume the following additional material parameters: Young's modulus $E = 100$ MPa; Poisson's ratio $v = 0.2$; hardening/softening modulus parameters $a_1 = 5000$, $a_2 = 0.0005$/kPa, and $a_3 = 50$; non-associativity parameter $\alpha = \kappa_2/\kappa_1 = 0.5$; and 'curving' parameters $m = 0.23$, and $p_a = -100$ kPa; for the MN model with $c_0 = 9$, we take $E = 100$ MPa; $v = 0.2$; $a_1 = 20000$; $a_2 = 0.005$/kPa; $a_3 = 35$; $\alpha = \kappa_2/\kappa_1 = 0.5$; $p_a = -100$ kPa; and $m = 0$ (no 'curving' effect). For both models the initial yield surface coincides with the hydrostatic axis and plastic deformation accumulates right at the onset of loading. Unless otherwise noted, initial stresses were $\sigma_1 = \sigma_2 = \sigma_3 = -200$ kPa on the hydrostatic line.

#### *5.1.1. Simple shearing with softening*

In this example a shear strain $\gamma_{12}$ was applied on the plane 1–2, holding the out-of-plane normal strain $\epsilon_{33}$ to zero and the two in-plane normal stresses $\sigma_{11}$ and $\sigma_{22}$ to their initial values. Thus, the problem determines the two in-plane normal strains $\epsilon_{11}$ and $\epsilon_{22}$ such that the resulting internal stresses balance the applied external stresses $\sigma_{11}$ and $\sigma_{22}$ under the plane strain condition $\epsilon_{33} = 0$. Figs. 7 and 8 show the variations of the shear stress $\sigma_{12}$ and the out-of-plane normal stress $\sigma_{33}$ as functions of the applied strain $\gamma_{12}$, assuming the material to be represented by the ML and MN models, respectively. For both models the 100- and 400-step solutions were practically identical. Softening responses were reached at shear strains of about 3%, accompanied by an increase in compression in the out-of-plane direction 3 (resulting primarily from dilation which, under the condition of zero strain in the direction 3, results in an increase in compression). Care must be taken in interpreting the calculated element responses as strain localization effects have not been considered in the analysis. It is possible for localized deformation to accompany a softening response, in which case the resulting element deformation will not be homogeneous. In this paper, we limit the scope of the study to the case where the element exhibits homogeneous deformations only.

#### *5.1.2. Biaxial compression with softening*

In this example the element was compressed in the two direction while holding $\sigma_1$ and $\sigma_3$ fixed. The results are plotted in Figs. 9 and 10 in the form of a deviator stress–axial strain curve for the ML and MN

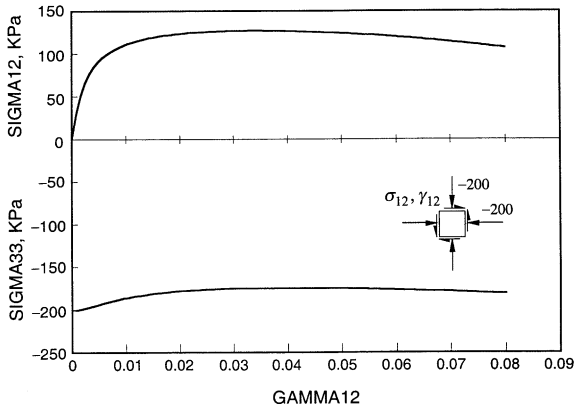


Fig. 7. Simple shear loading with softening using ML model.

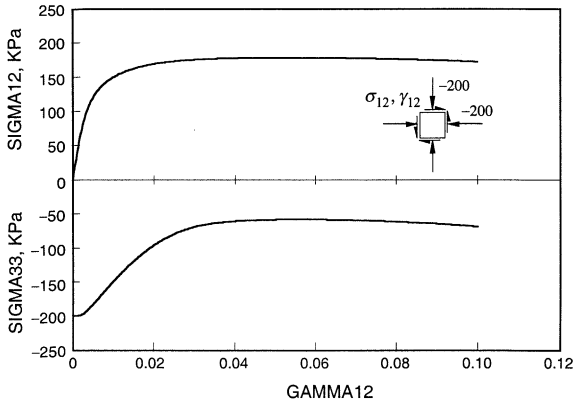


Fig. 8. Simple shear loading with softening using MN model.

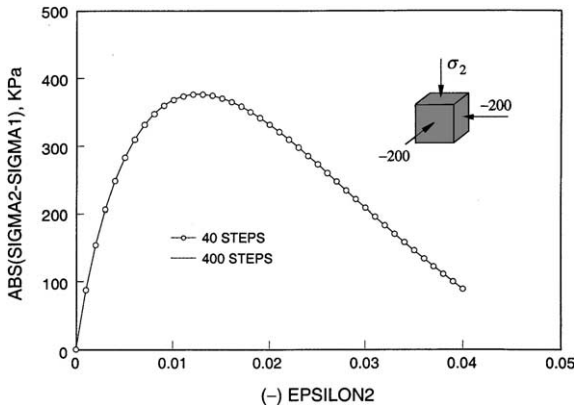


Fig. 9. Biaxial compression with softening using ML model.

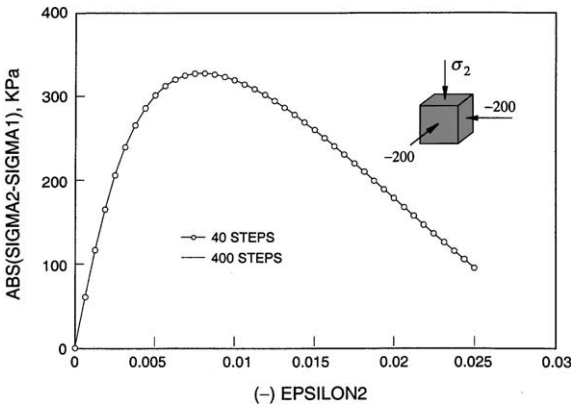


Fig. 10. Biaxial compression with softening using MN model.

simulations, respectively. Note that the softening response is far more prominent in biaxial compression than in simple shear simulation. Once again, the results shown in these figures only reflect material softening responses and do not include the effects of strain localization.

Both the eigenvector and eigenbasis approaches predicted the same responses to the applied loads with the smooth three-invariant models. Furthermore, both iterative approaches resulted in an asymptotic rate of quadratic convergence in Newton iteration, as shown in Figs. 11 and 12 for the simple shear and biaxial compression simulations, respectively. However, some sensitivity to time-stepping was noted in some of the runs. For example, neither the eigenvector nor the eigenbasis approach could converge in the biaxial compression example when fewer than 20 load increments were used. This could be due to how the repeated roots have been handled, or to the fact that the constitutive models are highly non-linear.

To get some insight into the accuracy of the algorithm, we constructed isoerror maps as described in [25]. Despite its lack of mathematical rigor, this procedure provides a quick numerical assessment of the accuracy of integration algorithms. In this section we limit our discussion to plane strain conditions in principal stress (or strain) space, i.e., $\epsilon_{33} = \epsilon_{12} = \epsilon_{23} = \epsilon_{13} = 0$. Starting from an isotropic compression state $\sigma_1 = \sigma_2 = \sigma_3 = -200$ kPa, we applied a series of strain increments and used the algorithm to calculate the corresponding stresses. Each combination of $(\Delta\epsilon_1, \Delta\epsilon_2)$ was prescribed in a single step. Next we calculated the 'exact' stresses resulting from the same strain increments by subdividing the increments until further refinement produces negligible changes in the calculated stresses. The relative error (mean root error) was calculated from the equation

$$\text{ERROR} = \frac{\sqrt{(\boldsymbol{\sigma} - \boldsymbol{\sigma}^*) : (\boldsymbol{\sigma} - \boldsymbol{\sigma}^*)}}{\sqrt{\boldsymbol{\sigma}^* : \boldsymbol{\sigma}^*}} \times 100\%, \tag{5.1}$$

where $\boldsymbol{\sigma}$ is the stress calculated with the given strain increments in one step, and $\boldsymbol{\sigma}^*$ is the corresponding 'exact' stress. Because, the testing of the algorithm in this case involves strain-driven loading and no constraints on the stresses, the algorithmic tangent plays no role in the calculation of error.

Fig. 13 shows isoerror maps for the ML and MN models, respectively. Due to the isotropy of the constitutive equations, the relative error is symmetric with respect to the biaxial compression line. For the ML model the relative error is less than 3.5% while that same error reduces to 1.4% or less for the MN model. Thus, at moderate strains the algorithm seems to provide good accuracy. We also mention that only the hardening regime is involved in the generation of the isoerror maps since it would be impractical to try to reach the softening regime in just one strain increment.

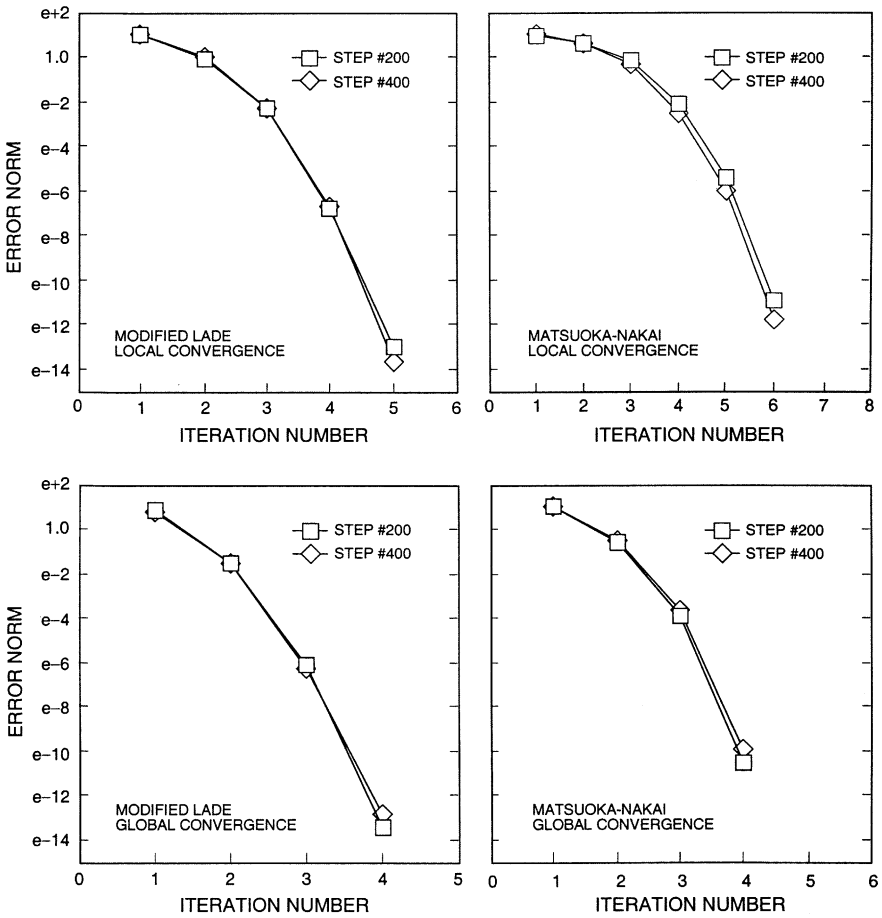


Fig. 11. Simple shear test with softening: local and global convergence of Newton iterations for ML and MN plasticity models.

### 5.2. Strip footing on frictional foundation

Next, we consider the classical strip footing problem on a frictional soil foundation. Due to vertical symmetry it suffices to consider only half of the domain. The finite element mesh is composed of 717 nodes and 1344 constant strain triangular (CST) elements deforming in plane strain, as shown in Fig. 14. The material parameters are assumed as follows: Young's modulus of elasticity $E = 5000$ kPa; Poisson's ratio $v = 0.30$; and exponential hardening parameters $a_1 = 0.02E$, and $a_2 = a_3 = 0$. Thus, the foundation soil hardens mildly according to the linear relation $\kappa_1 = a_1\lambda$. A non-associative flow rule is assumed, with $\alpha = \kappa_2/\kappa_1 = 0.5$ characterizing the plastic dilatational response. An initial friction angle of $\phi = 30°$ is assumed, and the parameter $m$ is taken equal to zero, i.e., the friction angle does not change with the confining pressure. The error tolerance was taken as $10^{-10}$ based on the $L_2$-norm of the residual force vector.

To get the solution started, gravity and initial surface loads were applied in one full step, with a soil unit weight $\gamma = 20$ kN/m$^3$ and a surface load of $q = 20$ kPa assumed in the analysis. For the LD model the assumed initial friction angle corresponds to an initial value of $k_1 = 38.11$, assuming that the yield surface passes through the tension corners, while for the MN model the corresponding initial value is $k_1 = 11.67$. With $v = 0.30$ the initial stress points lie inside the yield functions everywhere for either model. A uniform

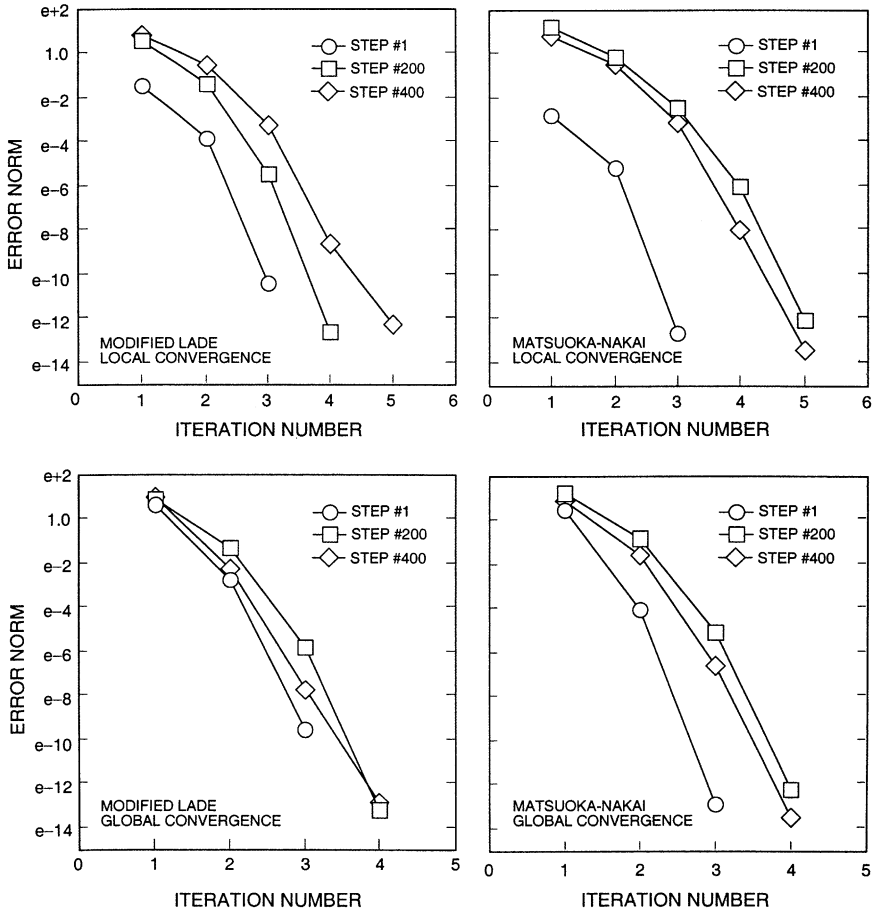


Fig. 12. Biaxial compression with softening: local and global convergence of Newton iterations for ML and MN plasticity models.

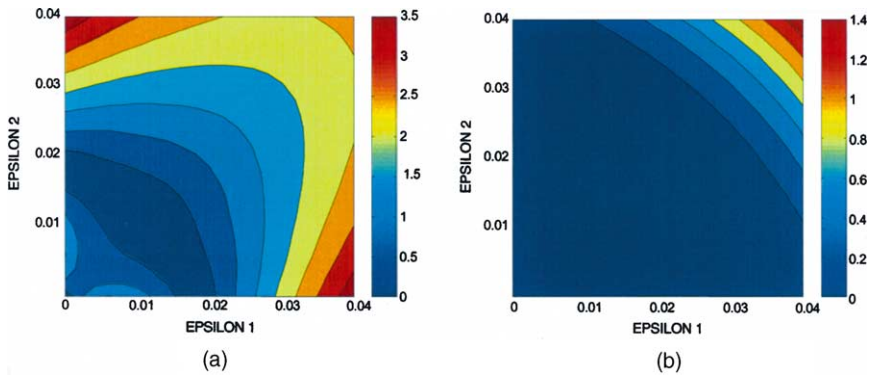


Fig. 13. Isoerror maps: (a) ML model; (b) MN model.

strip load $\Delta q = 200$ kPa was then applied in increments over a foundation half-width of 5 m, and initial plastic yielding of the foundation was observed to occur at a cumulative incremental footing load of

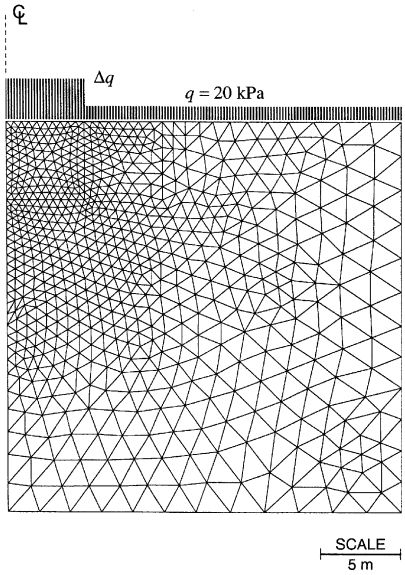


Fig. 14. Undeformed finite element mesh for strip footing example.

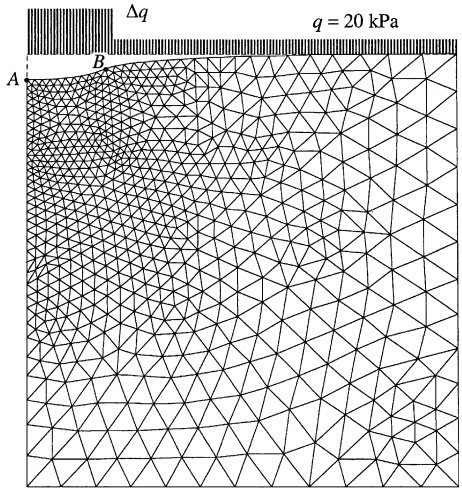


Fig. 15. Deformed finite element mesh for strip footing example.

$\Delta q = 12$ kPa for the LD model and $\Delta q = 20$ kPa for the MN model (the earlier yielding in the LD simulation was due to a smaller elastic region predicted by the yield surface that passes through the tension corners).

Fig. 15 shows the deformed mesh at the conclusion of the simulations. Here, $\Delta q$ was applied in 50 or 100 loading increments, and the two sets of numerical solutions for nodal displacements are compared at points $A$ (center line) and $B$ (edge of the strip load) on the ground surface. The numerical values of these displacements are summarized in Table 1. In general, the two sets of solutions are nearly identical, attesting to the accuracy of the algorithm. We note once again that the above solutions do not account for a possible

Table 1
Accuracy of numerical integration for strip footing example, infinitesimal plasticity case ($\Delta q = 200$ kPa)

| Plasticity model | 50 steps | 100 steps |
|---|---|---|
| *Panel a: vertical displacement at point A, m* | | |
| LD | −2.59510 | −2.59484 |
| MN | −2.45176 | −2.45169 |
| *Panel b: horizontal displacement at point B, m* | | |
| LD | −0.38834 | −0.38845 |
| MN | −0.38965 | −0.38965 |
| *Panel c: vertical displacement at point B, m* | | |
| LD | −1.71573 | −1.71609 |
| MN | −1.64886 | −1.64890 |

Table 2
Convergence profile of Newton iteration for the strip footing problem using the LD plasticity model: $L_2$-norm of the residual force vector at step number 20 of the 100-step solution

| Iteration number | Eigenvector[a] | Eigenbasis[a] | Eigenbasis[b] |
|---|---|---|---|
| 0 | 0.154e+02 | 0.154e+02 | 0.154e+02 |
| 1 | 0.353e+01 | 0.305e+01 | 0.305e+01 |
| 2 | 0.564e−01 | 0.112e−00 | 0.729e−01 |
| 3 | 0.134e−03 | 0.258e−03 | 0.144e−03 |
| 4 | 0.135e−05 | 0.165e−05 | 0.983e−06 |
| 5 | – | – | – |

[a] Eigenvalues/eigenvectors/eigenbases calculated from EISPACK routines [17,18].
[b] Eigenvalues/eigenbases calculated from closed-form solution [16].

Table 3
Convergence profile of Newton iteration for the strip footing problem using the MN plasticity model: $L_2$-norm of the residual force vector at step number 20 of the 100-step solution

| Iteration number | Eigenvector[a] | Eigenbasis[a] | Eigenbasis[b] |
|---|---|---|---|
| 0 | 0.154e+02 | 0.154e+02 | 0.154e+02 |
| 1 | 0.579e+00 | 0.583e+00 | 0.807e+00 |
| 2 | 0.801e−02 | 0.790e−02 | 0.816e−02 |
| 3 | 0.269e−05 | 0.179e−05 | 0.315e−05 |
| 4 | 0.571e−08 | 0.404e−08 | 0.683e−08 |
| 5 | – | – | – |

[a] Eigenvalues/eigenvectors/eigenbases calculated from EISPACK routines [17,18].
[b] Eigenvalues/eigenbases calculated from closed-form solution [16].

bifurcation and localization of deformation, which could occur with a non-associative plasticity model even in the hardening regime. The latter issue is currently under investigation in the context of three-invariant models and will be addressed in a separate publication.

Tables 2 and 3 compare the convergence profiles of Newton iteration for simulations with the LD and MN models, respectively. Here, the tangent operator constructed with the eigenvector approach utilized (2.18), while the tangent operator constructed with the eigenbasis approach was based on (2.13). Also, the latter tangent operator was evaluated in two ways, using the EISPACK routine described in Section 2.2 and the closed-form solution via the program PRINC on p. 762 of [16]. The accompanying tables show no apparent difference noted in the performance of the three algorithms, and all algorithms predicted the same structural responses.

### 5.3. Re-analysis of strip footing problem with finite deformation effects

As a final example, we consider the effects of finite deformation on the frictional foundation problem of the previous example. All of the data were the same as in the previous example, including the finite element mesh, material parameters, initial condition, and the imposed loads. The objective of the present example is merely to investigate the performance of the two tangent operators presented in Section 4.2, so we only focus on the convergence profiles exhibited by the eigenbasis and eigenvector iterative solutions utilizing the tangent operators (4.11) and (4.23), respectively.

The deformed mesh has the profile similar to that shown in Fig. 15, in which the middle node $A$ displaces vertically downward and the edge node $B$ also moves downward as well as displaces to the left. At an incremental footing load of $\Delta q = 100$ kPa applied in 50 increments, the predicted movements of the two nodes are summarized in Table 4. In all cases identical final displacements are obtained using the two tangent operators.

Table 5 compares the $L_2$-norms generated by the two tangent operators during the early part of loading (step number 5) when the material was still behaving elastically and only geometric non-linearities were present. Note that the $L_2$-norms for both iterations are identical up until the third iteration when round-off errors start to manifest in the solutions. This, together with the fact that they both produced identical final displacements, proves that the tangent operators constructed from the eigenvector and eigenbasis approaches are numerically the same, save for round-off errors. However, it is clear from the third iteration of Table 5 that the simpler calculations required by the eigenvector approach have resulted in smaller round-off errors, allowing the relative $L_2$-norm to reach a value as small as $0.345 \times 10^{-10}/0.154 \times 10^{2} = \mathrm{O}(10^{-12})$, when the relative $L_2$-norm produced by the more detailed calculations of the eigenbasis approach could not go below $\mathrm{O}(10^{-10})$.

Table 4
Accuracy of numerical integration for strip footing example, finite deformation plasticity case ($\Delta q = 100$ kPa)

| Plasticity model | Eigenvector | Eigenbasis |
|---|---|---|
| *Panel a: vertical displacement at point A, m* | | |
| LD | −1.23134 | −1.23134 |
| MN | −1.21749 | −1.21749 |
| *Panel b: horizontal displacement at point B, m* | | |
| LD | −0.24794 | −0.24794 |
| MN | −0.24470 | −0.24470 |
| *Panel c: vertical displacement at point B, m* | | |
| LD | −0.83314 | −0.83314 |
| MN | −0.83162 | −0.83162 |

Table 5
Convergence profile of Newton iteration for the strip footing problem during the hyperelastic phase of finite deformation analysis: $L_2$-norm of the residual force vector at step number 5 of the 100-step solution

| Iteration number | Eigenvector | Eigenbasis |
|---|---|---|
| 0 | 0.154e+02 | 0.154e+02 |
| 1 | 0.783e−01 | 0.783e−01 |
| 2 | 0.878e−06 | 0.878e−06 |
| 3 | 0.345e−10 | 0.255e−08 |
| 4 | – | – |

Table 6
Convergence profile of Newton iteration for the strip footing problem using the LD hyperelastic–plastic model with finite deformation effects: $L_2$-norm of the residual force vector at step number 50 of the 100-step solution

| Iteration number | Eigenvector | Eigenbasis |
|---|---|---|
| 0 | 0.154e+02 | 0.154e+02 |
| 1 | 0.469e+01 | 0.459e+01 |
| 2 | 0.178e+00 | 0.191e+00 |
| 3 | 0.138e−03 | 0.184e−03 |
| 4 | 0.883e−09 | 0.956e−08 |
| 5 | – | – |

Table 7
Convergence profile of Newton iteration for the strip footing problem using the MN hyperelastic–plastic model with finite deformation effects: $L_2$-norm of the residual force vector at step number 50 of the 100-step solution

| Iteration number | Eigenvector | Eigenbasis |
|---|---|---|
| 0 | 0.154e+02 | 0.154e+02 |
| 1 | 0.122e+01 | 0.113e+01 |
| 2 | 0.891e−02 | 0.913e−02 |
| 3 | 0.603e−06 | 0.649e−06 |
| 4 | 0.462e−10 | 0.188e−07 |
| 5 | – | – |

Tables 6 and 7 compare the same $L_2$-norms at a more advanced stage of loading (step number 50) when both material and geometric non-linearities were present, again using the three-invariant LD and MN constitutive models. Quadratic convergence is obtained in both cases, albeit the presence of material non-linearities required one extra iteration to reach convergence. Unlike the results shown in Table 5 where the $L_2$-norms are numerically the same, the $L_2$-norms are now only approximately the same with the eigenvector and eigenbasis calculations due primarily to the round-off errors that have propagated from the early part of the analyses. Nevertheless, we see that even in the plastic regime the eigenvector approach still produced slightly smaller relative $L_2$-norms (and smaller round-off errors) compared to the eigenbasis approach. From this standpoint, and from the point of view of relative ease in the numerical implementation, we advocate the use of the eigenvector approach to handle the spin of principal axes for the numerical integration of the three-invariant elastoplastic models considered in this paper.

## 6. Closure

We have implemented a numerical integration algorithm for a class of three-invariant elastoplastic constitutive models for frictional materials using a spectral representation of stresses and strains and a return mapping in principal stress directions. The technique accommodates the spin of principal stress or strain axes the discrete evolution of which is consistently linearizable in the context of Newton iteration. With regard to the specific form of the spin component of the algorithmic tangent operator, the eigenvector and eigenbasis approaches appear to be at par in handling the non-linearities of the constitutive model and geometric deformation, although the eigenvector approach is simpler to implement and thus produces smaller round-off errors.

As a further motivation for this work, we recall that the approach taken in this study has significant advantages over the traditional explicit and semi-implicit approaches still used for numerically integrating

advanced elastoplastic constitutive models for frictional materials (see e.g., [26,27]). Apart from the numerical stability of the backward implicit approach, the advantages of the proposed technique include the fact that: (1) no subincrementation is required by the algorithm; (2) for a stress increment originating inside the yield surface and finally landing on the yield surface, the algorithm does not require identification of the initial contact point on the yield surface; (3) no correction is needed for a yield surface drift since with convergence the stress point will never drift from the yield surface; and (d) the formulation readily can be generalized to the finite deformation regime. The trade-off is the implicit nature of the technique, but the algorithm has available closed-form expressions for the consistent tangent operator, so the implicit nature of the algorithm should have no adverse effect on its efficiency. Finally, for non-linear elasticity typical in geomaterials the algorithm may simply be reformulated so that the return mapping is carried out in principal strain directions, as advocated in [19,28,29].

## Acknowledgements

We are grateful to Dr Claudio Tamagnini for providing helpful insights into the implementation of the proposed algorithm, as well as to the anonymous reviewers for their constructive reviews. This work is supported in part by a grant from National Science Foundation under contract numbers CMS-9613906 and CMS-0201317 through the direction of Dr C.S. Astill. The second author acknowledges a National Science Foundation graduate research fellowship; the third author acknowledges a research assistantship through the National Performance of Dams Program (NPDP) at Stanford University.

## Appendix A. Relationships among the MC/LD/MN model parameters

To reduce the yield criteria to more recognizable forms, we transform the coordinate axes according to the sequence of rotations shown in Fig. 16. First, a positive rotation of $\pi/4$ about the $\sigma_2$-axis creates a transformation $(\sigma_1, \sigma_2, \sigma_3) \to (\sigma'_1, \sigma'_2, \sigma'_3)$; then, a negative rotation of $\theta = \cos^{-1}\sqrt{2/3}$ about the $\sigma'_1$-axis produces a transformation $(\sigma'_1, \sigma'_2, \sigma'_3) \to (\sigma''_1, \sigma''_2, \sigma''_3)$. This results in a rotated axis $\sigma''_3$ coinciding with the space diagonal. The sequence of rotation is described mathematically by the transformation matrices

$$\begin{Bmatrix} \sigma_1 \\ \sigma_2 \\ \sigma_3 \end{Bmatrix} = \begin{bmatrix} \sqrt{2}/2 & 0 & \sqrt{2}/2 \\ 0 & 1 & 0 \\ -\sqrt{2}/2 & 0 & \sqrt{2}/2 \end{bmatrix} \begin{bmatrix} 1 & 0 & 0 \\ 0 & \sqrt{2/3} & 1/\sqrt{3} \\ 0 & -1/\sqrt{3} & \sqrt{2/3} \end{bmatrix} \begin{Bmatrix} \sigma''_1 \\ \sigma''_2 \\ \sigma''_3 \end{Bmatrix}. \tag{A.1}$$

We thus have

$$I_1 = \sigma_1 + \sigma_2 + \sigma_3 = \sqrt{3}\sigma''_3 \tag{A.2}$$

for the first invariant,

$$I_2 = \sigma_1\sigma_2 + \sigma_2\sigma_3 + \sigma_1\sigma_3 = (\sigma''_3)^2 - \tfrac{1}{2}[(\sigma''_1)^2 + (\sigma''_2)^2] \tag{A.3}$$

for the second invariant, and

$$I_3 = \sigma_1\sigma_2\sigma_3 = \frac{\sqrt{3}}{9}(\sigma''_3)^3 + \frac{\sqrt{6}}{18}(\sigma''_2)^3 - \frac{\sqrt{6}}{6}\sigma''_2(\sigma''_1)^2 - \frac{\sqrt{3}}{6}\sigma''_3(\sigma''_1)^2 - \frac{\sqrt{3}}{6}\sigma''_3(\sigma''_2)^2 \tag{A.4}$$

for the third stress invariant.

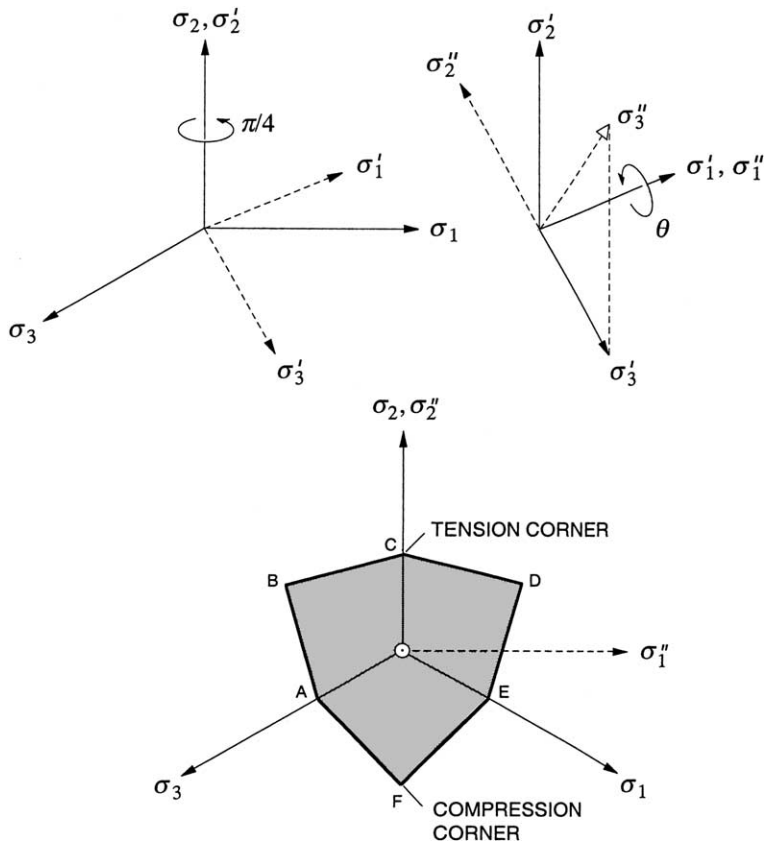


Fig. 16. Sequence of rotation of principal stress axes and representation of MC yield surface on the deviatoric plane.

Assuming a cohesion $c = 0$, the six hyperplanes of the MC yield function are given in the transformed coordinates by

$$
\begin{aligned}
&F(\sigma_1, \sigma_3) : \sqrt{2}\sigma_1'' \pm \left( \sqrt{\frac{2}{3}}\sigma_2'' - \frac{2}{\sqrt{3}}\sigma_3'' \right) \sin\phi = 0, \\
&F(\sigma_2, \sigma_3) : \frac{\sqrt{2}}{2}\sigma_1'' + \sqrt{\frac{3}{2}}\sigma_2'' \pm \left( \frac{\sqrt{2}}{2}\sigma_1'' - \frac{1}{\sqrt{6}}\sigma_2'' - \frac{2}{\sqrt{3}}\sigma_3'' \right) \sin\phi = 0, \\
&F(\sigma_1, \sigma_2) : \frac{\sqrt{2}}{2}\sigma_1'' - \sqrt{\frac{3}{2}}\sigma_2'' \pm \left( \frac{\sqrt{2}}{2}\sigma_1'' + \frac{1}{\sqrt{6}}\sigma_2'' + \frac{2}{\sqrt{3}}\sigma_3'' \right) \sin\phi = 0.
\end{aligned}
\tag{A.5}
$$

Setting $\sigma_1'' = 0$ gives the equations for the tension and compression corners of the MC yield function as

$$
\begin{aligned}
\sigma_2'' &= -\frac{2\sqrt{2}\sin\phi}{3 + \sin\phi}\sigma_3'' \quad \text{for a tension corner;} \\
&= \frac{2\sqrt{2}\sin\phi}{3 - \sin\phi}\sigma_3'' \qquad \text{for a compression corner,}
\end{aligned}
\tag{A.6}
$$

where $\sigma_3'' < 0$.

Consider now the LD yield function, $I_1^3/I_3 - k_1 = 0$. In the transformed coordinates the yield function writes

$$3(\sigma_1'')^2\left(\sqrt{2}\sigma_2'' + \sigma_3''\right) - (\sigma_2'')^2\left(\sqrt{2}\sigma_2'' - 3\sigma_3''\right) - 2(\sigma_3'')^3\left(\frac{k_1 - 27}{k_1}\right) = 0. \tag{A.7}$$

Setting $\sigma_1'' = 0$ and dividing by $(\sigma_3'')^3$ gives the relation

$$k_1 = \frac{27}{1 - \eta^2(3 - \sqrt{2}\eta)/2}, \quad \eta = \frac{\sigma_2''}{\sigma_3''}, \quad \sigma_3'' \neq 0. \tag{A.8}$$

The stress ratio $\eta$ may be chosen such that the yield function passes through either the tension or compression corners of the MC hexagon, i.e.,

$$\eta = \begin{cases} -2\sqrt{2}\sin\phi/(3 + \sin\phi) & \text{for tension corner;} \\ 2\sqrt{2}\sin\phi/(3 - \sin\phi) & \text{for compression corner.} \end{cases} \tag{A.9}$$

The final results are

$$k_1 = \frac{(3 + \sin\phi_t)^3}{1 + \sin\phi_t - \sin^2\phi_t - \sin^3\phi_t} \tag{A.10}$$

for a yield surface passing through the tension corners, and

$$k_1 = \frac{(3 - \sin\phi_c)^3}{1 - \sin\phi_c - \sin^2\phi_c + \sin^3\phi_c} \tag{A.11}$$

for a yield surface passing through the compression corners. The inverse expressions for $\sin\phi_t$ and $\sin\phi_c$ as functions of $k_1$ are given in (3.22) and (3.23), respectively.

The MN yield function, $I_1 I_2/I_3 - k_1 = 0$, writes in the transformed coordinates as

$$3(\sigma_1'')^2[(k_1 - 3)\sigma_3'' + \sqrt{2}k_1\sigma_2''] - 3(3 - k_1)(\sigma_2'')^2\sigma_3'' - 2(k_1 - 9)(\sigma_3'')^3 - \sqrt{2}k_1(\sigma_2'')^3 = 0. \tag{A.12}$$

Setting $\sigma_1'' = 0$ and dividing by $(\sigma_3'')^3$ gives the relation

$$k_1 = \frac{18 - 9\eta^2}{\sqrt{2}\eta^3 - 3\eta^2 + 2} = \frac{9\sqrt{2} + 9\eta}{-\sqrt{2}\eta^2 + \eta + \sqrt{2}}, \tag{A.13}$$

where $\eta$ is as defined in (A.8). The yield function passes through the tension and compression corners of the MC hexagon when (A.9) is substituted into (A.13). Either of the two expressions for $\eta$ gives

$$k_1 = \frac{9 - \sin^2\phi}{1 - \sin^2\phi}. \tag{A.14}$$

The inverse expression for $\sin\phi$ as a function of $k_1$ is given in (3.30).

## References

[1] J. Jiang, S. Pietruszczak, Convexity of yield loci for pressure sensitive materials, Comput. Geotech. 5 (1988) 51–63.
[2] P.V. Lade, J.M. Duncan, Elastoplastic stress–strain theory for cohesionless soil, J. Geotech. Engrg. Div., ASCE 101 (1975) 1037–1053.
[3] H. Matsuoka, T. Nakai, Stress-deformation and strength characteristics of soil under three different principal stresses, Proc. JSCE 232 (1974) 59–70.
[4] J.H. Argyris, G. Faust, J. Szimmat, E.P. Warnke, K.J. Willam, Recent developments in the finite element analysis of prestressed concrete reactor vessel, Nuclear Engrg. Des. 28 (1974) 42–75.

[5] K.J. Willam, E.P. Warnke, Constitutive model for the triaxial behaviour of concrete, ISMES Seminar on Concrete Structures Subjected to Triaxial Stresses, Bergamo, Italy, 1975, pp. 1–30.
[6] L.F. Boswell, Z. Chen, A general failure criterion for plain concrete, Int. J. Solids Struct. 23 (1987) 621–630.
[7] P.V. Lade, Elasto-plastic stress–strain theory for cohesionless soil with curved yield surfaces, Int. J. Solids Struct. 13 (1977) 1019–1035.
[8] J.C. Simo, Algorithms for static and dynamic multiplicative plasticity that preserve the classical return mapping schemes of the infinitesimal theory, Comput. Meth. Appl. Mech. Engrg. 99 (1992) 61–112.
[9] J.C. Simo, Numerical analysis and simulation of plasticity, in: P.G. Ciarlet, J.L. Lions (Eds.), Handbook of Numerical Analysis, vol. VI, North Holland, The Netherlands, 1998, pp. 183–499.
[10] W.T. Koiter, Stress–strain relations, uniqueness and variational theorems for elastic–plastic materials with a singular yield surface, Quart. Appl. Math. 11 (1953) 350–354.
[11] R.W. Ogden, Nonlinear Elastic Deformations, Chichester, Ellis Horwood, 1984.
[12] T.C.T. Ting, Determination of $\boldsymbol{C}^{1/2}$, $\boldsymbol{C}^{-1/2}$ and more general isotropic functions of $\boldsymbol{C}$, J. Elasticity 15 (1985) 319–323.
[13] K.N. Morman, The generalized strain measure with application to non-homogeneous deformation in rubber-like solids, J. Appl. Mech. 53 (1986) 726–728.
[14] C. Miehe, Aspects of the formulation and finite element implementation of large strain isotropic elasticity, Int. J. Numer. Meth. Engrg. 37 (1994) 1981–2004.
[15] C. Miehe, Comparison of two algorithms for the computation of fourth-order isotropic tensor functions, Comput. Struct. 66 (1998) 37–43.
[16] T.J.R. Hughes, The Finite Element Method, Prentice-Hall, Englewood Cliffs, NJ, 1987.
[17] B.N. Parlett, The Symmetric Eigenvalue Problem, Prentice-Hall, Englewood Cliffs, NJ, 1980.
[18] B.T. Smith, J.M. Boyle, Y. Ikebe, V.C. Klema, C.B. Moler, Matrix Eigensystem Routines: EISPACK Guide, 2nd Ed., Lecture Notes in Computer Science, vol. 6, Springer, New York, 1976.
[19] C. Tamagnini, R. Castellanza, R. Nova, A generalized backward Euler algorithm for the numerical integration of an isotropic hardening elastoplastic model for mechanical and chemical degradation of bonded geomaterials, Int. J. Numer. Anal. Meth. Geomech. 26 (2002) 963–1004.
[20] J.C. Simo, J.G. Kennedy, S. Govindjee, Non-smooth multisurface plasticity and viscoplasticity. Loading/unloading conditions and numerical algorithms, Int. J. Numer. Meth. Engrg. 26 (1988) 2161–2185.
[21] R.I. Borja, J.R. Wren, Discrete micromechanics of elastoplastic crystals, Int. J. Numer. Meth. Engrg. 36 (1993) 3815–3840.
[22] R.I. Borja, Plasticity Modeling and Computation, Lecture Notes, Stanford University, California, 2001.
[23] J. Sulem, I. Vardoulakis, E. Papamichos, A. Oulahna, J. Tronvoll, Elasto-plastic modelling of Red Wildmoor sandstone, Mech. Cohesive-Frictional Mater. 4 (1999) 215–245.
[24] M. Ortiz, J.B. Martin, Symmetry-preserving return mapping algorithms and incrementally extremal paths: a unification of concepts, Int. J. Numer. Meth. Engrg. 28 (1989) 1839–1853.
[25] J.C. Simo, T.J.R. Hughes, Computational Inelasticity, Springer, New York, 1998.
[26] P.V. Lade, K.P. Jakobsen, Incrementalization of a single hardening constitutive model for frictional materials, Int. J. Numer. Anal. Meth. Geomech. 26 (2002) 647–659.
[27] K.P. Jakobsen, P.V. Lade, Implementation algorithm for a single hardening constitutive model for geomaterials, Int. J. Numer. Anal. Meth. Geomech. 26 (2002) 661–681.
[28] R.I. Borja, C. Tamagnini, Cam-Clay plasticity. Part III. Extension of the infinitesimal model to include finite strains, Comput. Meth. Appl. Mech. Engrg. 155 (1998) 73–95.
[29] R.I. Borja, C.H. Lin, F.J. Montáns, Cam-Clay plasticity. Part IV. Implicit integration of anisotroic bounding surface model with nonlinear hyperelasticity and ellipsoidal loading function, Comput. Meth. Appl. Mech. Engrg. 190 (2001) 3293–3323.